12-2017

Finite Element Analysis of Tibiofemoral Contact Mechanics

Erika Fojtik
Western Michigan University, e.foitik94@gmail.com

FINITE ELEMENT ANALYSIS OF TIBIOFEMORAL CONTACT MECHANICS

by

Erika Fojtik

A thesis submitted to the Graduate College
in partial fulfillment of the requirements
for the degree of Master of Science in Engineering
Mechanical
Western Michigan University
December 2017

Thesis Committee:

Peter Gustafson, Ph.D., Chair
Daniel Kujawski, Ph.D.
Andrew Geeslin, M.D.

FINITE ELEMENT ANALYSIS OF TIBIOFEMORAL CONTACT MECHANICS

Erika Fojtik, M.S.E.

Western Michigan University, 2017

The effects of lateral meniscus posterior root avulsions (LMPRA) have been studied in combination with meniscofemoral ligament (MFL) deficiencies. The purpose of this study is to validate a set of biomechanical finite element analyses against previously reported experimental results to predict the contact area and peak contact pressure in the lateral tibiofemoral compartment of the knee during lateral meniscal root avulsions in combination with MFL deficiencies. Patient specific MRI data was used to develop finite element models for three distinct testing conditions: 1) intact, 2) lateral meniscus posterior root avulsion, and 3) lateral meniscus posterior root avulsion with deficient meniscofemoral ligaments. The model of each condition will maintain a fixed flexion angle of 0° under a 1,000 N compressive load. This work was compared against patient specific experimental data which proved to show agreeable results. The computational model reported results of 446 mm^2 for contact area and 2.84 MPa for peak contact pressure at condition 1 – intact. These results were 14% less compared to those from the experimental study when comparing contact area and 22% less for peak contact pressure. Condition 2 – LMPRA – yielded contact area of 356 mm^2 and 2.89 MPa for peak contact pressure. Contact area came in 32% less than the experimental data and the peak contact pressure was reported at 12% less. For condition 3 – LMPRA with deficient MFLs – contact area came in at 310 mm^2 and peak contact pressure was 2.98 MPa. These results were only 2% more than the experimental data for contact area but 35% less for the peak contact pressure. These results clearly show that the MFL has major stabilizing effects for the knee when a LMPRA is present. While surgical intervention is the common approach to the occurrence of a LMPRA even with the presence of MFLs, this work confirms that the MFLs will add a secondary stabilizer in the knee against injury.

ACKNOWLEDGMENTS

I would like to thank all of my friends, family, loved ones, coworkers, peers, and advisors for their support, encouragement, and kind words throughout my entire master's and higher education career.

Special thanks to Dr. Peter Gustafson and Dr. Andrew Geeslin for your guidance, patience, and passion for this work. It was a true pleasure to have the opportunity to work alongside and learn from both of you.

Erika Fojtik

TABLE OF CONTENTS

Table of Contents—Continued

LIST OF TABLES

LIST OF FIGURES

List of Figures—Continued

LIST OF EQUATIONS

CHAPTER 1 INTRODUCTION

1.1 The Meniscus

The meniscus is the fibrocartilaginous, crescent moon-shaped structure with roughly a wedge cross section that sits between the femur and tibia in the knee. Its main functions are to provide shock absorption, stability, and compliance between the two articulating surfaces of the femur and tibia [1]. The two menisci in the knee – the lateral (meaning to the outside) and medial (to the middle) – are shown in Figure 1. Circumferential, radial, and random fiber orientations dictate the load transmission through the body of the menisci, shown in Figure 2 [2]. The circumferential fibers carry the majority of the load by transferring the axial compressive stresses outward radially through the meniscus. This load then is distributed circumferentially around the meniscus in the form of tensile hoop stresses along the fiber direction. This interaction is shown in Figure 3. This allows for an even distributive load across the surface of the femur to the tibia. Any sort of injury or tear to the meniscus can leave the knee in an altered biomechanical state which over time can severely deteriorate the surfaces of the knee. Surgical intervention is almost always necessary.

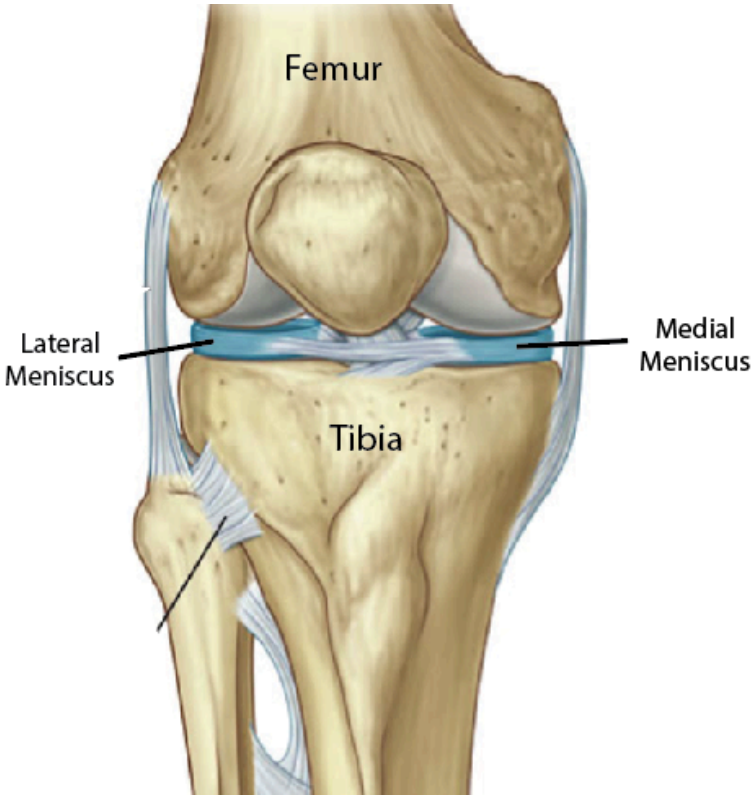

Figure 1: Anterior (front) view of left knee showing medial (middle) and lateral (outside) menisci. Base graphic from [3].

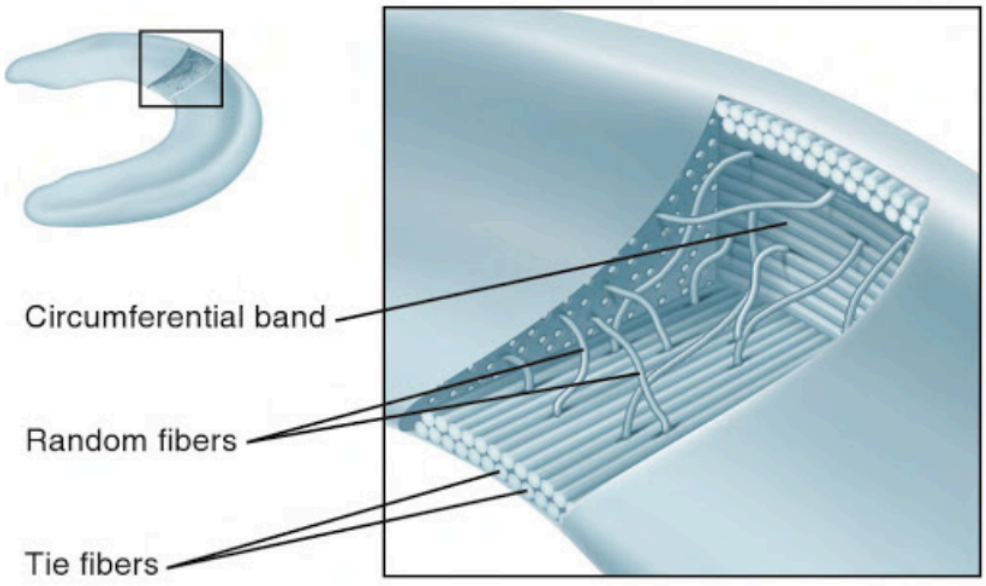

Figure 2: Pattern of collagen fibers in the meniscus [2].

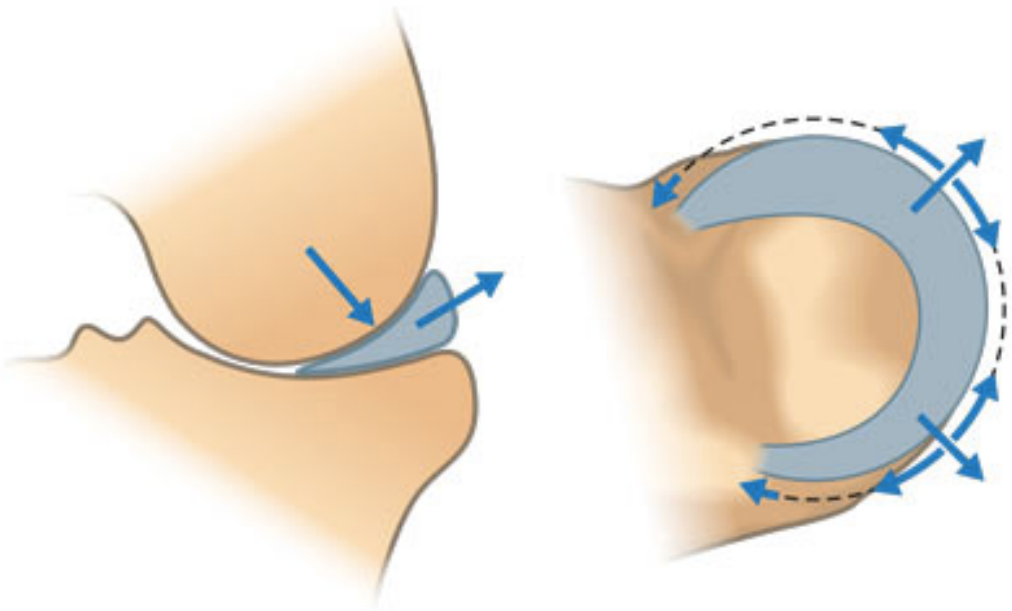

Figure 3: The meniscus helps to distribute load across the femur to the tibia by means of hoop stresses running circumferentially along the axis of the meniscus [4].

1.2 Meniscal Root Tears

The roots of the meniscus, which act as the anchors of the meniscus, attach into the surface of the tibia. Each meniscus has an anterior (front) and posterior (back) attachment point, shown in Figure 4. If a root becomes torn, or avulsed, the ability of the meniscus to carry load is virtually all lost. This change in load distribution from an intact, healthy joint load to an injured state is shown in Figure 5. This shows that for an intact meniscus, even load distribution across the femur is transferred through the meniscus to the surface of the tibia. When the root is torn, this load distribution is lost and becomes nearly a point load from surface to surface. Most weight is transmitted through the posterior sections of the menisci, and therefore is why it is more common to see posterior root avulsions [2]. Typically, a root avulsion is due to trauma from sports, such as those with pivot-contact, for younger people. Additionally, it has been reported that anywhere from to 8% to 17% of anterior cruciate ligament (ACL) tears have a combined posterior lateral root tear [5-7]. In the older population, low-energy squatting or deep flexion positions can cause a posterior root tear to occur [8]. Meniscus extrusion, or the meniscus extending outside its normal anatomical placement between bones, is a common symptom of root tear and can be observed on magnetic resonance imaging, or MRI, to detect meniscal root tears pre-operatively. A study showed that for a medial posterior meniscus root tear, the biomechanical response to joint loading was effectively the same as that of a total meniscectomy, or the total surgical removal of the meniscus [9]. This type of altered biomechanical response causes long term damage in the form of osteoarthritis, or joint deterioration, due to the increased contact pressures across the femoral and tibial cartilages, which cover the articulating surfaces of the femur and tibia, respectively. Because of their link of altered tibiofemoral contact mechanics to the progression of osteoarthritis, the study of meniscal root injury and repair is of increased interest [10 11].

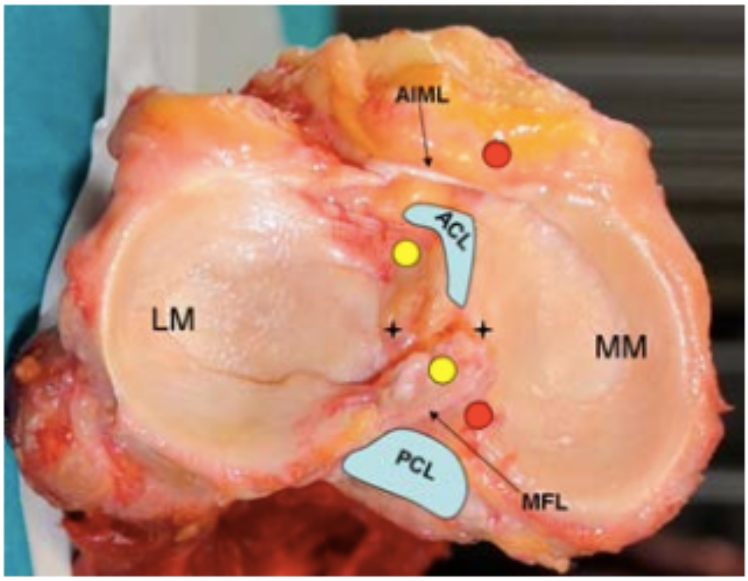

Figure 4: Anatomy of medial meniscus (MM) and lateral meniscus (LM) with their attachment points shown with red and yellow dots, respectively. Black stars show the apex of the medial and lateral intercondylar eminence. Anterior cruciate ligament (ACL); posterior cruciate ligament (PCL); Anterior intermeniscal ligament (AIML); Meniscofemoral ligament (MFL) [11].

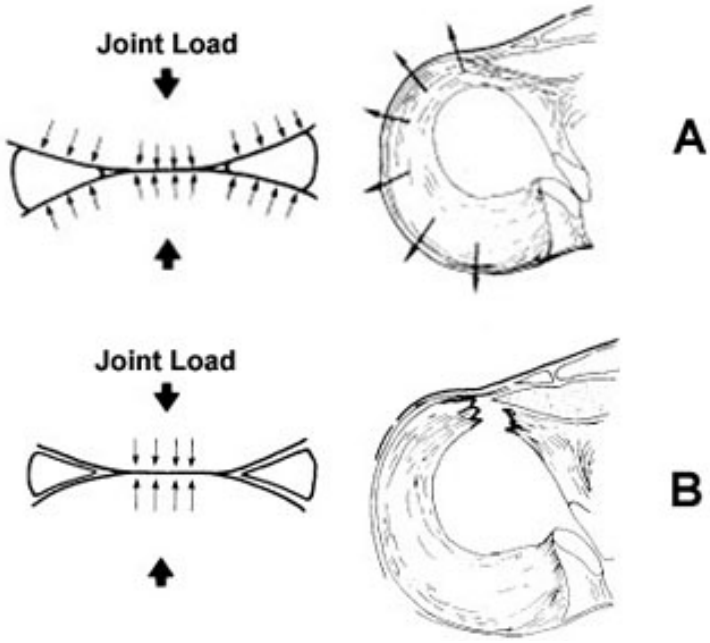

Figure 5: A) Menisci act to distribute load evenly between the femur and tibia when intact. B) The biomechanical response to loading is altered when meniscus becomes damaged, such as a root avulsion. This effectively becomes a point load from surface to surface [12].

1.3 Surgical Techniques

Portions of the meniscus are avascular, or lacking of blood supply, as seen in Figure 6. Therefore, self-healing is not possible to heal a tear in the avascular portions of the meniscus. Surgical intervention must take place in order to regain near-intact biomechanical contact. Meniscal root tears are defined by being within 1 cm of the meniscal root insertion site [13]. LaPrade et al developed a classification system to identify tears of the meniscal roots [10]. Type 2 meniscal root tears, shown in Figure 7, are defined as complete radial tears within 9mm of the center of the root attachment and are the type of tear which are of interest in this study [10].

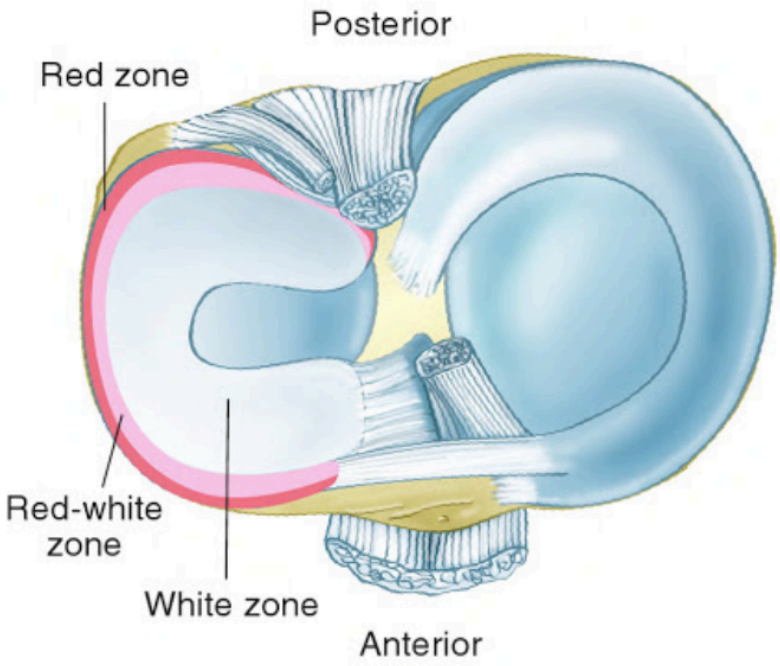

Figure 6: The three "blood supply zones" of a meniscus - red, red-white, white. Tears in the red zone have good healing potential due to the presence of a blood supply. Tears in the red-white zone have limited healing potential. Tears in the white zone, or avascular portion, usually require partial meniscectomy [2].

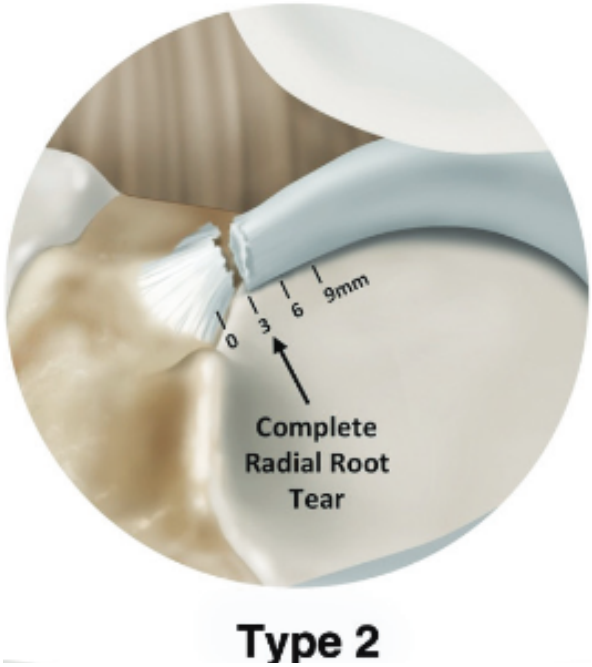

Figure 7: Based on the classification system developed by LaPrade et al, a Type 2 meniscal root tear - complete radial tear within 9 mm from the bony root attachment [10].

While treatment varies by many factors such as age, progression of osteoarthritis, and more, the most common surgical repair technique is the transtibial pull-out repair for an avulsed meniscal root [1 9 10 14]. This technique has clearly been found to restore contact mechanics after repair [14]. Such a technique is shown in Figure 8. This technique is accomplished by passing a suture through the torn root and then passing it through a drilled tunnel in the tibia bone. From there, the sutures are terminated to a button which sits on top of the anterior aspect of the tibia [10]. In order to restore meniscal function and allow for best healing, adequate tensioning on the suture and anatomical placement of the tunnels are critical [1].

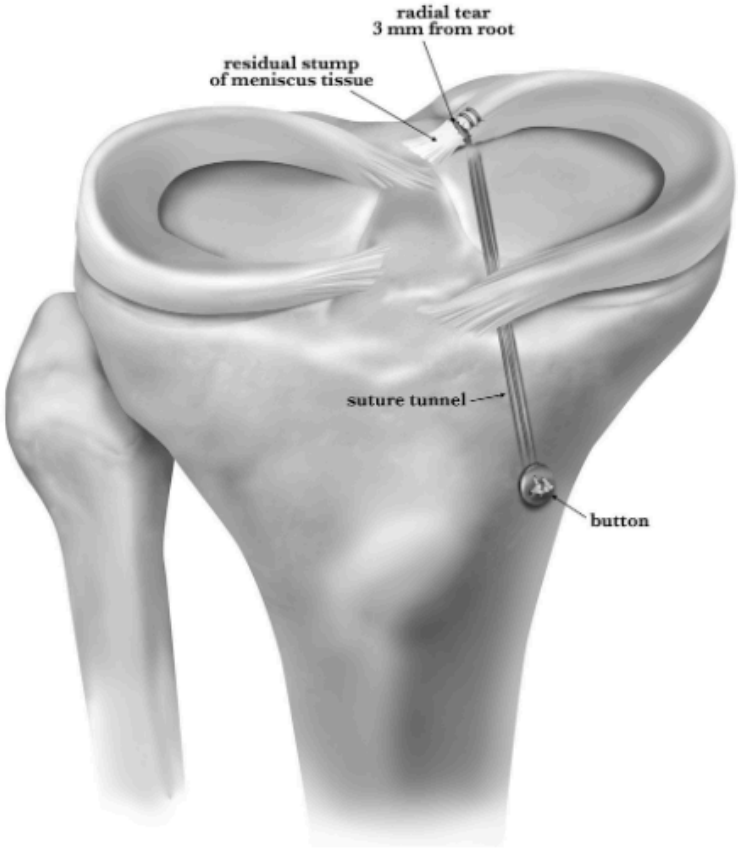

Figure 8: Transosseous (through bone) suture repair tied over a button on the anteromedial tibia [1].

1.4 The Meniscofemoral Ligaments

Two lesser known, but distinct, ligaments in the knee are the meniscofemoral ligaments (MFLs). These include the anterior meniscofemoral ligament (aMFL), known as the ligament of Humphrey, and the posterior meniscofemoral ligament (pMFL), known as the ligament of Wrisberg [15]. The MFLs are bands of collagen that attach at the lateral meniscus posterior horn and insert onto the intercondylar area of the femur running parallel with the PCL. The aMFL extends anterior to the posterior cruciate ligament (PCL) while the pMFL extends posterior to the to the PCL, as their names suggest. This orientation can be discreetly seen in Figure 9 where the lateral femoral condyle has been cut away to assist in the viewing of the MFLs with respect to

the PCL. Figure 10 shows two views posteriorly, for the pMFL only, of an illustration and a cadaver. The aMFL was also present in the cadaveric knee, but is not seen in this image.

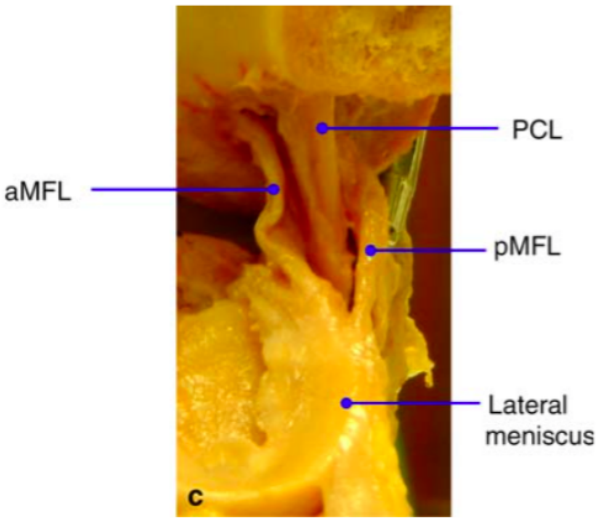

Figure 9: The two MFLs attach from the posterior lateral meniscus horn. The aMFL extends anterior to the PCL and the pMFL extends posterior to the PCL. The lateral femoral condyle has been removed for easier viewing [15].

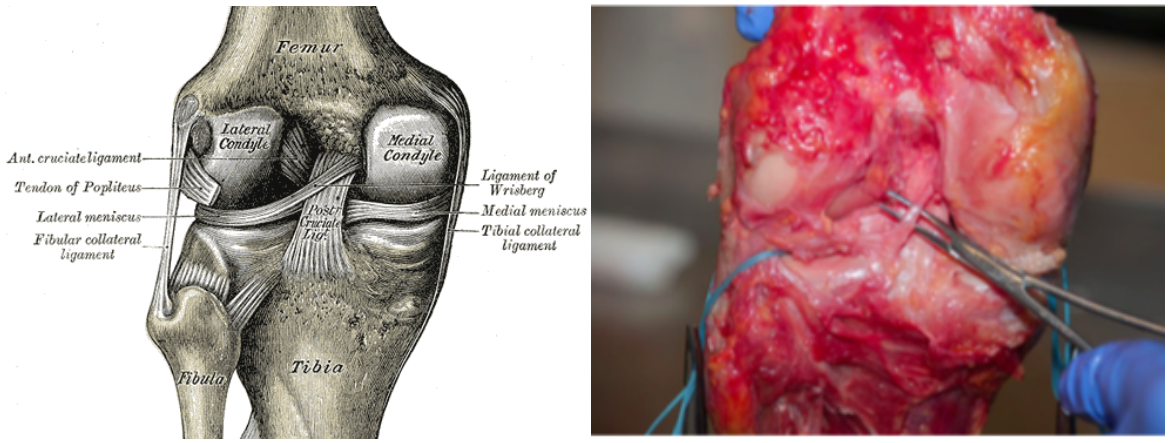

A) B)

Figure 10: A) Illustration of the knee showing the pMFL, or Ligament of Wrisberg [16]. B) Cadaver knee with a curved surgical instrument to allow for the identification of the pMFL to be seen. The aMFL was also present in this specimen but not seen in this image [17].

These ligaments become of great interest due to their known tendency of being missing, or deficient, in some patients. For instance, in a study done by Bintoudi et al which performed MRI evaluations on 500 knees to identify the presence of aMFL and pMFL, only 37% of the patients had both ligaments present, with a higher percentage present in male patients (54%) in comparison to female (46%) [18]. Another study by Gupte et al showed that in a sample size of 84 cadaveric knees, 93% of the specimen contained at least one MFL with 74% showing the presence of the aMFL and 69% had the pMFL present [19]. It should be noted that 50% of the specimen for which both ligaments were present, a significant amount were from a younger population (mean age of 54.1 +/- 20.8) compared to the those with one or no MFLs present (66.2 +/- 18.8 years) [19]. Both of these studies found good agreement that older subjects were less likely to exhibit both MFLs [18 19]. This leads to some speculation as to whether MFLs disappear over time after injury or from osteoarthritis deterioration.

It is also significant to note the vast differences in MFL size and shape. Figure 11 shows four different shapes that the pMFL took shape in specimen. These size differences may have biomechanical significance, though not studied to a great extent.

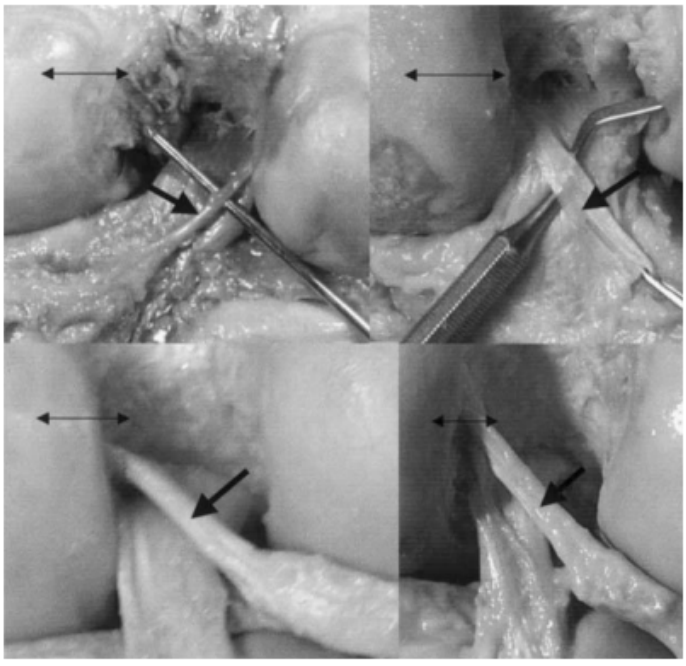

Figure 11: The meniscofemoral ligaments (pMFL in image) can take many different shapes and sizes in specimen. Width of the midsubstance of the PCL is indicated with the double headed arrow [19].

While the function of the MFLs are not entirely known, there is some evidence to support their ability to help keep in place the posterior root of the lateral meniscus. For example, the patients in the study done by Bintoudi were all admitted for MRI examination due to either chronic pain or trauma to the knee. The lower percentage of patients having both ligaments present could relate to their incidence of injury, indicating that the MFLs act as a significant stabilizing structure in the knee and hold biomechanical advantages when present. Figure 12 shows how even with a posterior lateral meniscus root tear, the present pMFL acts as an additional anchor point.

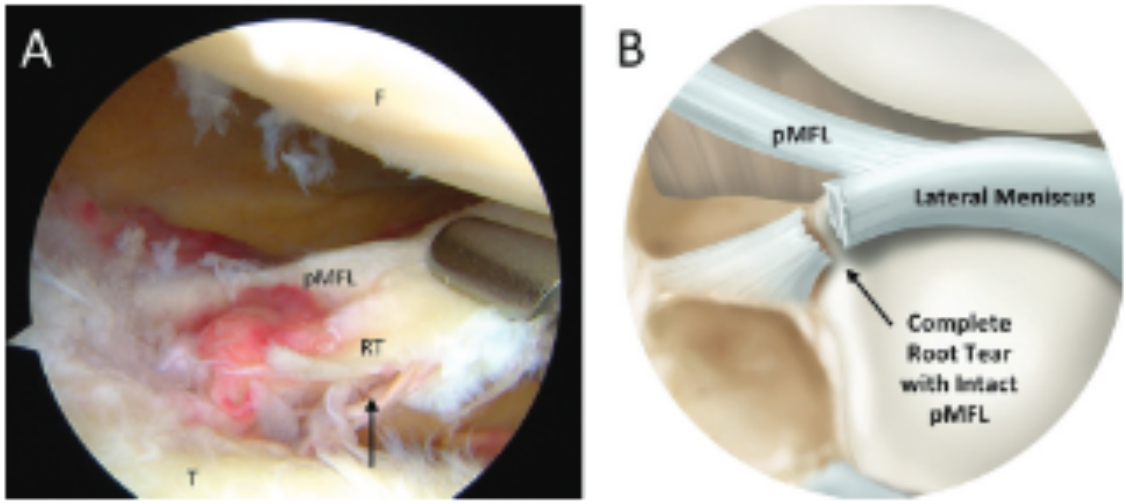

Figure 12: (A) Arthroscopic image and (B) illustration of a complete tear of the posterior lateral meniscal root (arrow) and the stabilizing effect of the pMFL. F, Femur, RT, Root Tear; T, Tibia [10].

A study by Geeslin et al compared the contact area and pressure of an intact knee against several conditions related to a lateral meniscus posterior root avulsion and MFL deficiencies [17]. Ten Cadaver knees were loaded axially at multiple flexion angles and the contact mechanics were recorded in the joint. They compared contact area and pressures on the tibial cartilage surface – a well-accepted and commonly used metric for studying tibiofemoral contact mechanics. They found in the ten knees that compared to intact, or condition 1 at 0° (538 mm^2), contact area in the lateral compartment of the knee decreased by 8% (495 mm^2) for LMPRA, or condition 2, and decreased by 37% (339 mm^2) for LMPRA and deficient MFL, condition 3 [17]. The peak contact pressure increased from intact (2.77 MPa) by 6% (2.94 MPa) for condition 2 and by 28% (3.55 MPa) for condition 3 [17]. This trend continued when flexion angles were increased from 0° to

90°. This shows that compared to intact condition, an LMPRA (condition 2) with the presence of one or both of the MFLs in the knee maintains near intact contact mechanics when observing pressure and area compared to when a LMPRA is coupled with deficient MFLs. This interaction caused the contact area to decrease sharply and pressure to steeply increase. This clearly shows a relationship between the role that the MFLs has to play in the presence of LMPRA. This phenomenon has also been observed experimentally in a number of studies similar to that of the Geeslin study [9 14 20].

1.5 Objective and Thesis Summary

The objective of this thesis is to develop and validate a set of biomechanical finite element (FE) models of the knee to investigate and predict the contact mechanics during lateral meniscal root avulsions in combination with meniscofemoral ligament (MFL) deficiencies. This study aims to look at the contact area and peak pressures present during these conditions and validate the results against the findings from the Geeslin study. One of the ten cadaveric knees used in the Geeslin study will be used to develop the model used in the finite element analysis (FEA). This will be done by using MRI of the knee provided at 0° flexion and by making use of segmentation tools to create the 3D model. Conditions 1, 2, and 3 will be compared against for the purposes of this work. Once validated, the model will be able to explain to a greater extent the role of which the MFLs have in constraining the LMPR in loading. This work plays a significant role in providing surgeons with better decision making tools and understanding of the consequences of surgical repair techniques done to the lateral meniscus posterior root. Additionally, this work will provide a model which can be used to further explore the other knee loading conditions outlined in the Geeslin study such as dynamic axial loading, rotational loads, and shear stresses in order to better understand the stabilizing effects of the MFLs. This study proves its uniqueness by its patient specific modeling and comparison to real data gathered experimentally. Additionally, advanced modeling techniques and powerful FEA tools will be utilized to provide the most representative results.

Chapter 2 includes a concise literature review, outlining other studies which are similar in nature to the one at hand. This will also provide context to some of the assumptions and decisions that were made in the development of this model. Chapter 3 outlines the materials and methods of the Geeslin study and how those play into the current project by clearly explaining the steps that were taken in the preprocessing portion of the modeling as well as the tools used to solve the FEA. Chapter 4 will describe the results of the FEA, showing both contact area and peak contact pressures and show the comparisons against the experimental study. Chapter 5 will discuss the results further, their significance, and talk in depth about the findings. Lastly, Chapter 6 summarizes the work and lays out recommendations and future work.

CHAPTER 2 LITERATURE REVIEW

The goals of this thesis are similar to other studies which developed FE models of knee joints. The development of specific MRI and CT interpretation software has made segmentation the preferred method to begin the development of a 3D model of a knee. Segmentation essentially allows a user to separate individual components out of an image scan in order to use in a 3D modeling environment. Even though Donahue et al did not use segmentation software to develop a model, but rather a 3D laser coordinate digitizing system, their basic processes and methodology prove to be legitimate and still present in today's studies [21]. Their study aimed to understand what changes in contact occur during partial and total meniscectomy. Their output metrics included peak contact pressure, mean contact pressure, and contact area. This was done by applying a 1,200 N compressive load at 0˚ flexion. While the results were intuitive – removing portions of the meniscus increased contact pressures and reduced contact areas, due to its dated software and 3D modeling capabilities, this lacked in its ability to produce quantitative results that held much value. Bao et al also did a study which looked at contact pressures and areas after applying a compressive axial load of 1,000 N on the joint [22]. Their study, which did use MRI segmentation to create the 3D model, had similar goals when it came to the different conditions at which the models were created. This study looked at intact, LMPRA, and deficient MFLs. Their study produced agreeable results with those gathered by the Geeslin study and to other studies reported in the literature. Where this study lacked was its inability to validate the numbers gathered against real, patient specific experimental values. Instead, they compared their values *only* against other similar studies in the literature. Mootanah et al developed a 3D model to predict the contact forces and pressures in the knee for varying degrees of flexion [23]. This study also used MRI segmentation to develop the model but loaded the knee with a 374 N axial load as well as applied varus/valgus, or inward/outward, moment arms to the model. This study proved strong in its patient specific work against cadaver testing as well as its methodology to determining the material properties for the ligaments using a tuning approach. Where this study

lacked was its model's anatomical accuracy. Clear anatomical inaccuracies were noted and could be reason for yielding inaccurate results. Regardless, this study was able to validate its computational results against its experimental findings.

The commonalities and differences from these studies typically yield from the approach to material modeling. A summary of the materials used in the aforementioned studies in addition to other studies which proved very relevant are outlined in Table 1. Fundamentally, the strongest FE model's goal is to find the perfect combination of adequately representative material models while optimizing computational cost and result accuracy. The table shows with the depth and variety of materials used in these studies, that there is no clear winner to a successful model. This is especially true when dealing with biological models which add another level of complexity and variability when attempting to draw widespread conclusions for material models to use when there are so many factors that play into the specific values to use, such as age, gender, and availability of subjects to test among a few. It should be noted, that only a surface level referencing scheme was used for the summary table of materials. Ideally, a further investigation into each reference for which the material was chosen would be done in order to clearly identify the origination of the material properties used. The table does show some cross-linked references. But due to the scope of this project, that deep dive referencing scheme was left out. Additionally, it was noted that Abaqus was the common solver listed in the studies identified in the summarization. Abaqus is a well-known industry FEA tool and excels in its contact algorithms, which is the key to a successful knee model.

Table 1: Author comparison table of materials used to define model.

Author	***Software***	***Femur/Tibia Bone***	***Tibia/Femur Cartilage***	***Lateral/Medial Meniscus***	***Root attachment***	***Ligaments***
Donahue (2006) [21]	Abaqus	RB	Linear Elastic, Isotropic E =15MPa ν = 0.475	Linearly Elastic, Transversely Isotropic E_1 = 150 MPa $E_2 = E_3$ = 20 MPa $\nu_{12} = \nu_{13} = 0.3$ $\nu_{23} = 0.2$ G = 57.7 MPa	1D Springs	1D Springs
Kiapour (2014) [24]	Abaqus	Linear Elastic, Isotropic *Tibia* / *Femur* E_1 [MPa]: 69,000 / 12,000 E_2 [MPa]: 8,500 / 13,400 E_3 [MPa]: 18,400 / 20,000 ν_{12}: 0.49 / 0.38 ν_{13}: 0.12 / 0.22 ν_{23}: 0.14 / 0.24 Cortical bone: ρ = 2 g/cm^3 Trabecular bone: ρ = 1.5 g/cm^3 E = 400 MPa ν= 0.3	Linear Elastic, Isotropic ρ = 1 g/cm^3 E = 15 MPa ν= 0.475	Linear Elastic, Transversely Isotropic ρ = 1.5 g/cm^3 E_1 = 20 MPa E_2 =120 MPa E_3 = 20 MPa ν_{12}= 0.3 ν_{13}= 0.45 ν_{23}= 0.3	Linear Elastic, Isotropic E = 111 MPa ν= N/A	Hyperelastic, Holzapfel-Gasser-Ogden (HGO) model
Pena (2006) [25]	Abaqus	RB	Linear Elastic, Isotropic E = 5MPa ν= 0 .46	Linear Elastic, Isotropic E = 59 MPa ν= 0.49	Assumed no material difference between body and insertion	Hyperelastic, Neo-Hookean model
Mootanah (2014) [23]	Abaqus	Linear Elastic, Isotropic E=1,000 MPa ν= 0.3	Linear Elastic, Isotropic E = 25MPa ν = 0.45	Linear Elastic, Transversely Isotropic E_1 = 120 MPa $E_2 = E_3$ = 20 MPa $G_{12} = G_{13}$ = 57.7 MPa G_{23} = 8.33 MPa $\nu_{12} = \nu_{13}$= 0.3 ν_{23}= 0.2		Hyperelastic, Neo-Hookean model
Bao (2012) [22]	Abaqus	RB	Linear Elastic, Isotropic E = 15MPa ν= 0.47	Linear Elastic, Transversely Isotropic E_1 = 120 MPa $E_2 = E_3$ = 20MPa $\nu_{12} = \nu_{13}$= 0.2 ν_{23}= 0.3	Linear Elastic, Isotropic E = 120MPa ν = 0.45	Hyperelastic Neo-Hookean model

RB, Rigid Body; 1 = Radial, 2 = Circumferential, 3 = Axial.

2.1 Hyperelasticity Theory

Table 1 clearly showed that higher complexity material modeling methods were used for ligaments throughout the studies summarized. The ligaments are the bands of strong, flexible, connective tissue that connect bone to bone across joints. Mechanically, they assist our joints to help guide normal motion and resist undesired motion. These bands are made up of fiber bundles of collagen and elastin which act as the main provider of resistance to tensile loading in the ligament while offering no significant resistance to compression [26 27]. Nearly all biological soft tissues can be classified as anisotropic, viscoelastic, inhomogeneous, nearly incompressible materials [26]. Under normal and injured conditions, they will undergo large deformations in vivo, or taking place inside of a living organism. There are four main ligaments in the knee: the anterior cruciate ligament (ACL); posterior cruciate ligament, (PCL); medial collateral ligament (MCL); and lateral collateral ligament (LCL). Over the past 30 years, a wide variety of material models have been selected for studying the knee joint in computational finite element analysis (FEA). Both 1D, 2D, and 3D representations of the ligaments have been used with the understanding that 1D and 2D models yield low computational cost, with limited accuracy when the focus is that particular ligament. Additionally, the mechanism of ligament wrapping, when two crossing ligaments come into contact with each other, will be lost in the analysis [28]. The wrapping effect is most relevant when observing the knee at higher flexion angles other than full extension (0°). 3D, higher order models yield accurate but add to a higher overall computational cost. A balance must be met depending on the analyst's needs for any given job. For this study, 3D ligaments were used in the analysis in order to represent the most accurate physically interpreted results – with the downfall of high computational cost.

It is important to explain the two distinctive regions that become present in the force-strain curve created from tensile testing of a ligament. This trend is shown in Figure 13. This is divided into the toe region (blue) and linear region (beige). The toe region is the nonlinear portion of the curve, which stems from the fibers in the ligament beginning to un-crimp and reach a pre-tensioned state, shown in Figure 14. This region has low stiffness properties. The second region, the ‘linear region’, exhibits higher stiffness and is nearly linear. This corresponds to the fibers beginning to stretch, post un-crimping.

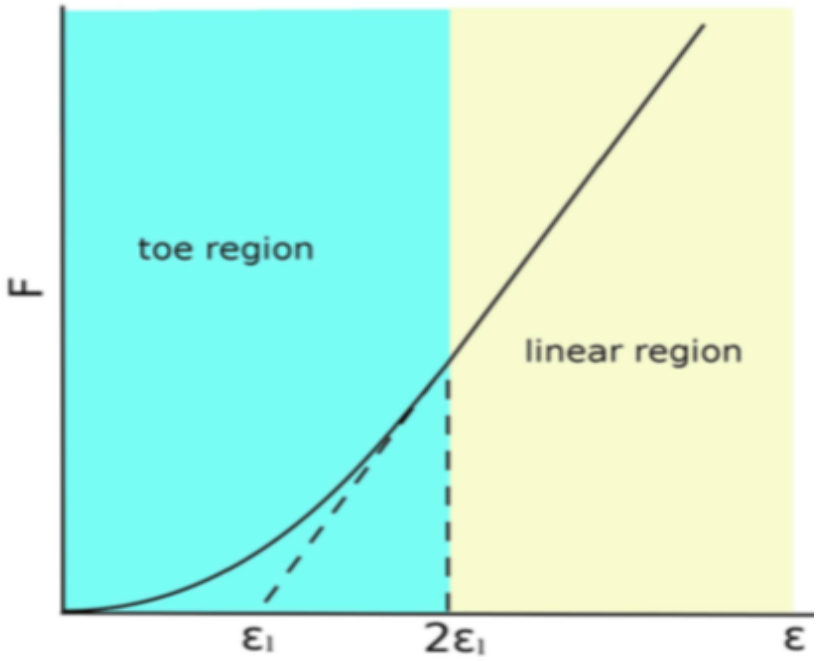

Figure 13: Force–strain behavior of a generic ligament. $2\varepsilon_1$ is the threshold strain, which indicates the change from the toe to the linear regions [29].

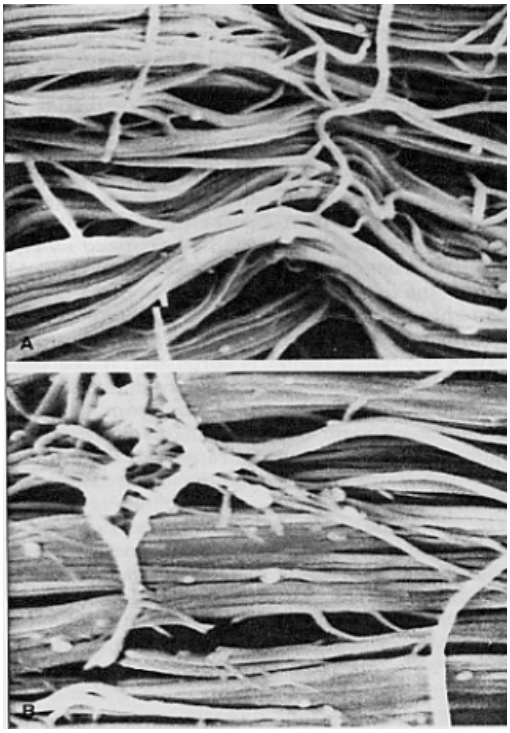

Figure 14: Fibers in a ligament during A) un-crimped, relaxed state and B) Pre-tension state [30].

Stress within linear elastic materials can be defined as a function of a deformation gradient at the point of interest − that is, the stress changes with a change of configuration and the material, independent to the way the change occurs in space and time [27]. Not all materials behave in such a linear manner, and therefore other material models must be used to accurately capture their behaviors. Hyperelastic material models depend on an additional scalar quantity to derive stress at any point in a body. This stems from the strain energy function of that body and must consist of constitutive equations that are invariant to any frame of reference under deformation [27]. Because of the non-linearity that is observed in ligament loading, hyperelastic models great candidates to represent the model most accurately. In practice, hyperelastic material models are typically used for polymers or rubbers.

Invariants, or the independence of a coordinate system, represent the coefficients of the characteristic polynomial of a tensor, in our case, *C*, in the Right Cauchy-Green Deformation Tensor. This value is the square of the local change in distances due to deformation,

Equation 1 $$C = F^T F = U^2$$

where, *F* is the deformation gradient and,

Equation 2 $$F = \frac{\partial x}{\partial X}$$

where, *x* is the coordinates of each point in current position and,
X is the coordinates of each point in initial position [31].

The first invariant (also known as the trace of the matrix) is always the sum of the diagonals of the matrix,

Equation 3 $$I_1 = tr(C) = C_{11} + C_{22} + C_{33} = \lambda_1^2 + \lambda_2^2 + \lambda_3^2$$

where λ_i are known as the principal stretches which represent the stretch in length between the fiber in the deformed and reference positions, i.e.,

Equation 4 $$\lambda_i = \frac{x_i}{X_i} = \frac{L}{L_0}.$$

Then,

Equation 5 $$I_2 = \frac{1}{2}\left(\left(tr(C)\right)^2 - tr(C^2)\right) = \lambda_1^2\lambda_2^2 + \lambda_2^2\lambda_3^2 + \lambda_3^2\lambda_1^2$$

and,

Equation 6 $$I_3 = detC = \lambda_1^2\lambda_2^2\lambda_3^2.$$

For incompressibility, $I_3 = 1$.

We now can say that the deformation gradient, *F*, is equal to:

Equation 7 $$F = \begin{bmatrix} \lambda_1 & 0 & 0 \\ 0 & \lambda_2 & 0 \\ 0 & 0 & \lambda_3 \end{bmatrix}$$ *[31].*

Many authors choose hyperelastic, neo-Hookean materials for their ligament modeling, mostly coming from the work done by Weiss et al [26] in 1996. As was mentioned, hyperelastic materials are functions of the materials strain energy density. Because of their complex nature, their material constants must be found experimentally through testing. The strain energy density equation is as follows for Neo-Hookean materials,

Equation 8 $$\Psi = \frac{1}{2D} ln\,(J)^2 + C_{10}(\bar{I}_1 - 3) + F_2(\lambda)$$ *[25]*

where F_2 is a function of the stretch. The Neo-Hookean material model utilizes experimental material constants, C_{10} and D, as well as the first invariant, I_1. The bulk modulus K_0 is related to D by,

Equation 9 $$D_1 = \frac{2}{K_0}$$

and the shear modulus, μ_0, is related to C_{10} by,

Equation 10 $$C_{10} = \frac{\mu_0}{2}.$$ *[22]*

Because of incompressibility limitations in the FEA solver used for this analysis, Calculix, the ratio of K_0/μ_0 must be chosen such that the Poisson's ratio is less than 0.48. Table 2 shows a K_0/μ_0 ratio table. Through interpolation, for a Poisson's ratio of 0.480, the K_0/μ_0 becomes 30. The original material constants are shown in Table 3. The new values of D were determined through numerical manipulation using Equation 9 and Equation 10 to fulfill this requirement. Authors such as Pena et al and Bao et al have used the same experimentally derived values from Table 3 in their analyses for 3D ligaments [22 25]. Because of the nearly exact biological makeup and biomechanical response to loading of the MCL and MFLs, these two ligaments utilize the same material constants for hyperelasticity. This is also relevant for the MCL and LCL.

Table 2: Relationship between compressibility and Poisson's ratio [32].

K_0/μ_0	Poisson's Ratio, ν
10	0.452
20	0.475
50	0.490
100	0.495
1,000	0.4995
10,000	0.49995

Table 3: Experimentally derived material properties used for ligaments (MPa) based on [22].

	C_1	C_2	C_3	C_4	C_5	λ^*	D
MCL	1.44	0	0.5700	48.00	467.100	1.063	0.00126
LCL	1.44	0	0.5700	48.00	467.100	1.063	0.00126
ACL	1.95	0	0.0139	116.22	535.039	1.046	0.00683
PCL	3.25	0	0.1196	87.178	431.063	1.035	0.00410
MFL	3.25	0	0.1196	87.178	431.063	1.035	0.00410

2.2 Contact

Modeling contact is one of the most difficult things to do in an FEA. The aim of this thesis is designed to predict the contact mechanics when compressive loads are incident upon the knee. Contact is essentially a nonlinear boundary condition that enforces the prevention of penetration between bodies as they begin to touch each other's surfaces. This is done through an iterative approach in the solver which continuously monitors for penetration and then therefore enforces a reactive pressure in response. Calculix, the solver used in this work, recommends that for quadratic elements, a face-to-face contact should be used [33], as demonstrated in Figure 15. This is due to the fact that as contact is initiated for a quadratic element, compressive forces will be applied to the midnodes of the elements and tensile forces will be applied to the vertex nodes, leading to major divergence issues in the solver. Contact can be described using a pressure-

overclosure relationship. In the case of a linear relationship, the pressure-overclosure can be described by Equation 11.

Equation 11 $$p = Kd\left[\frac{1}{2} + \frac{1}{\pi}tan^{-1}\left(\frac{d}{\epsilon}\right)\right]$$ *[33]*

The enforced pressure, *p,* is the response to the overclosure, or clearance, *d*. This is determined by the constant parameter, *K*, only (the parameter ϵ is not necessary) for face-to-face contact [33 34]. Stiffer contact can be created by use of a larger value of *K* and is typically anywhere between 5 to 50 times the Young's Modulus of the adjacent materials for the contact [33]. It should be noted that this equation is a true bilinear relationship, that is it is zero for no clearance between surfaces and then linear when penetration is initiated [34].

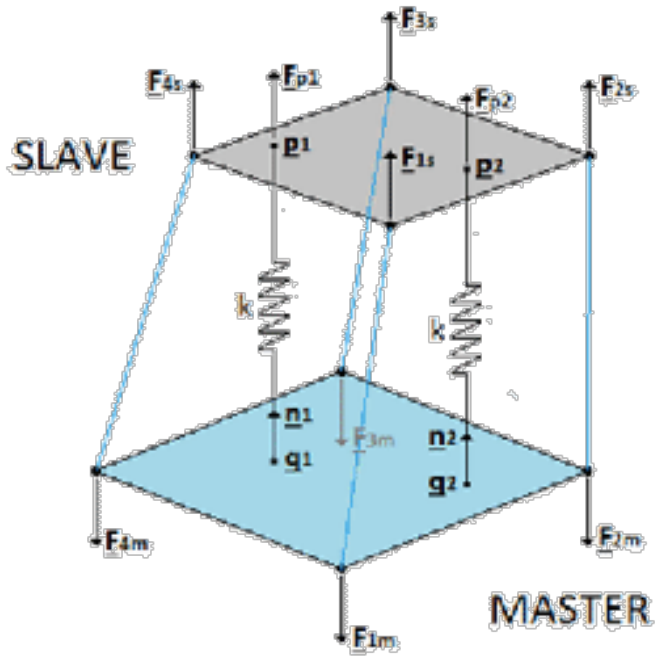

Figure 15: Face to face contact as represented by the solver, Calculix [34].

CHAPTER 3 MATERIALS AND METHODS

3.1 Experimental Analysis

The study done by Geeslin et al used ten fresh-frozen cadaveric knees to investigate the effects of LPMRA and the MFLs. All knees were noted to have intact menisci and at least one MFL present. An MRI scan from one of the ten knees prior to testing was used this project. Six different conditions were tested in the study:

(1) intact,
(2) LMPRA with intact MFLs,
(3) LMPRA with deficient MFLs,
(4) LMPRA, deficient MFLs, and a torn ACL,
(5) LMPRA, deficient MFLs, and a reconstructed ACL, and lastly,
(6) repaired LMPRA, deficient MFLs, and a reconstructed ACL [17].

Conditions 1, 2, and 3 were the only conditions of interest for the scope of this project, as demonstrated in Figure 18, Figure 17, Figure 18, respectively. Therefore, conditions 4, 5, and 6 were not further investigated. Additionally, Table 4 provides a key to outline each condition.

Table 4: Conditions key.

Condition	**Structure**	
	Lateral Meniscus Posterior Root	*Meniscofemoral Ligament(s)*
1	Intact	Intact
2	Avulsion	Intact
3	Avulsion	Deficient

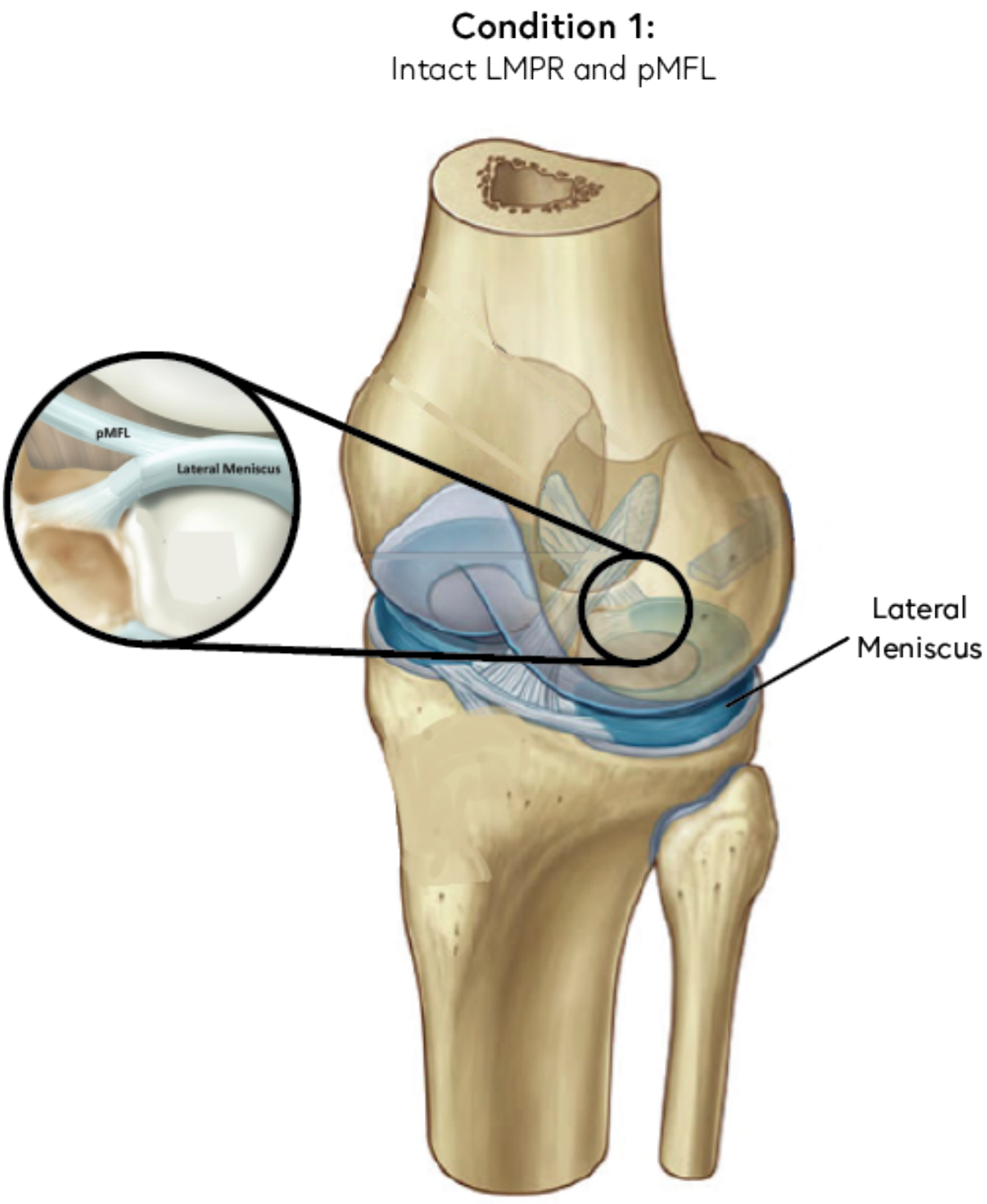

Figure 16: Condition 1 - Intact. Base images modified from [10] and [2].

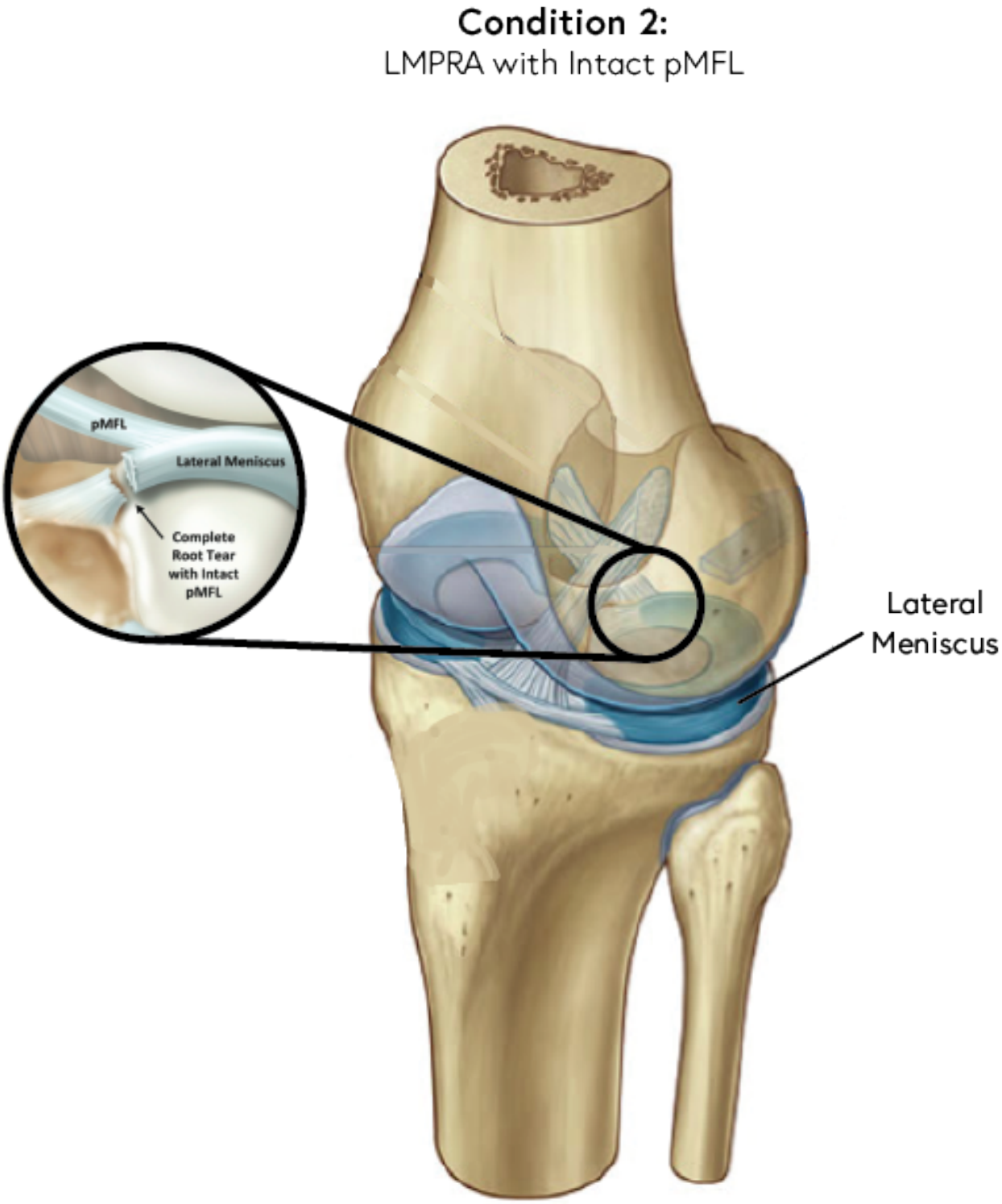

Figure 17: Condition 2 - Lateral meniscus posterior root avulsion (LMPRA). Base images modified from [10] and [2].

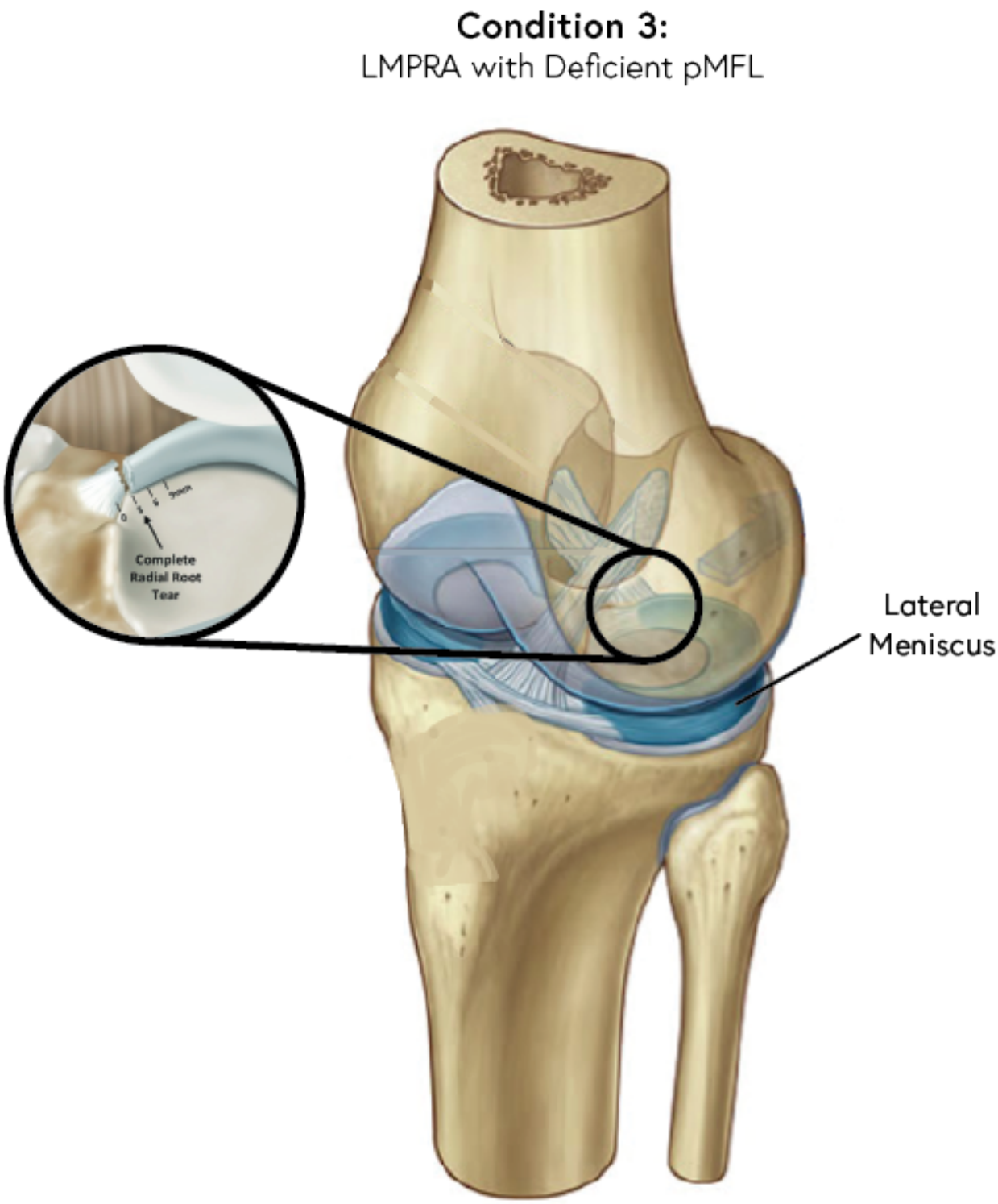

Figure 18: Condition 3 – Lateral meniscus posterior root avulsion and deficient pMFL. Base images modified from [10] and [2].

An axial load of 1,000 N was applied along the femur for 30s of constant application at five flexion angles: 0°, 30°, 45°, 60°, and 90°. Because the MRI provided from this study was only at a 0° flexion, the scope of the FE model was restricted to only this flexion angle (0°). Additionally, unknowns related to ligament pre-tensioning at the other flexion angles provided further reasoning to limit this work to only 0° flexion. In the experimental study, both tibia and fibula were potted in polymethylmethacrylate (PMMA) for stability and ease of handling. This also helped to keep the tibia and fibula in correct relative space to each other distally. The proximal femur was inserted into a loading jig where two metal bars running along the sagittal axis controlled flexion angle, as seen in Figure 19. The femur side provided the load application from a force-displacement cell. The potted distal end of the tibia was assembled into custom fixturing that allowed for fine tuning of varus, or inward, and valgus, or outward angulation, as seen in Figure 20. This setup also allowed for freedom of translation and rotation. The main reasoning behind this setup was to have the ability to observe the behavioral reactions for the ACL loading conditions. For the purposes of conditions that don't alter the ACL, these degrees of translational freedom could have been constrained, and that was the approach used for the computational model.

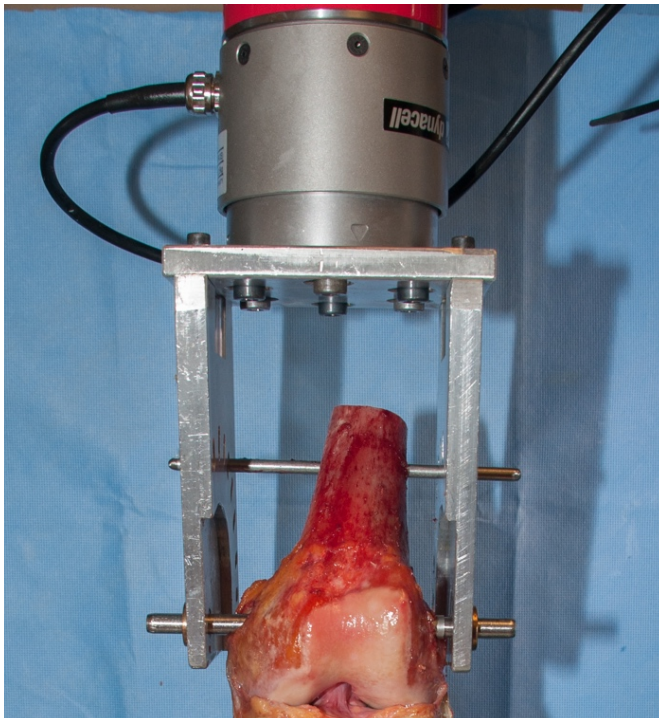

Figure 19: Femur side loading apparatus.

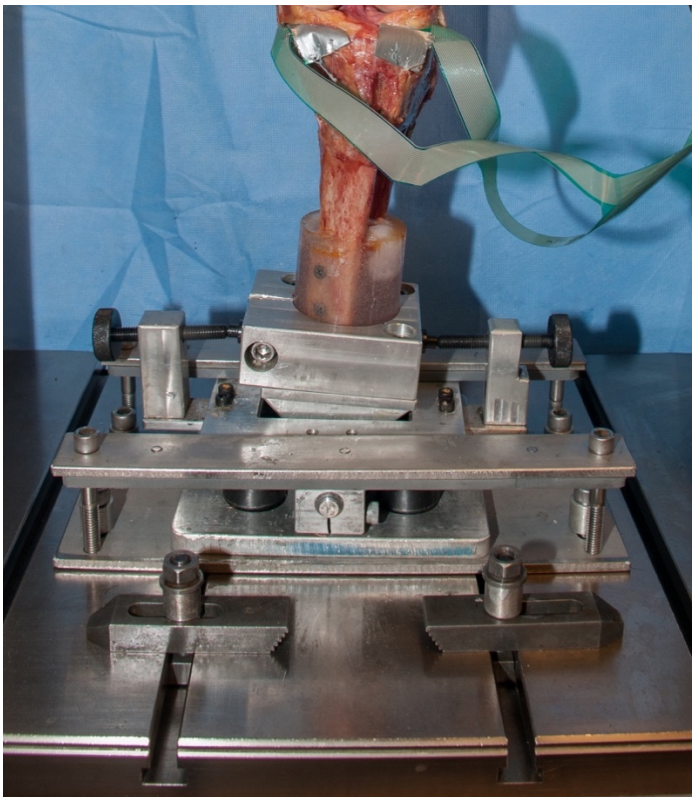

Figure 20: Tibia side fixturing apparatus.

Contact pressure mapping and peak pressure were measured using a Tekscan pressure mapping sensor (Model 4000, South Boston, Massachusetts) – an industry standard in this type of biomechanical testing [35]. The sensors are shown schematically in Figure 21. This sensor was placed between the menisci and the tibial cartilage on both compartments of the knee, lateral and medial. This is shown in Figure 22. Additionally, the footprint of this sensor on the tibial cartilage is shown from an axial view in Figure 23. The scanner is able to determine pressure by discretizing the contact area into sub-sensors, which are called sensels. In the flexible circuit, sandwiched between sets of electrodes is a semiconductor material that is piezoresistive. This material will change resistivity when a force is applied on it [36]. Knowing the area of that sensel measuring the force, a pressure can be interpreted from the measured resistively change through the simple pressure equation of $P=F/A$. The scanner has a resolution of 22 x 26 sensels over a 27.9 x 33 mm area. The datasheet from this scanner is outlined in Table 5. Results from the scanner were gathered after the end of the 30s of applied load and interpreted for analysis. The area of the sensors was directly used to measure the same area on the computational model for consistency.

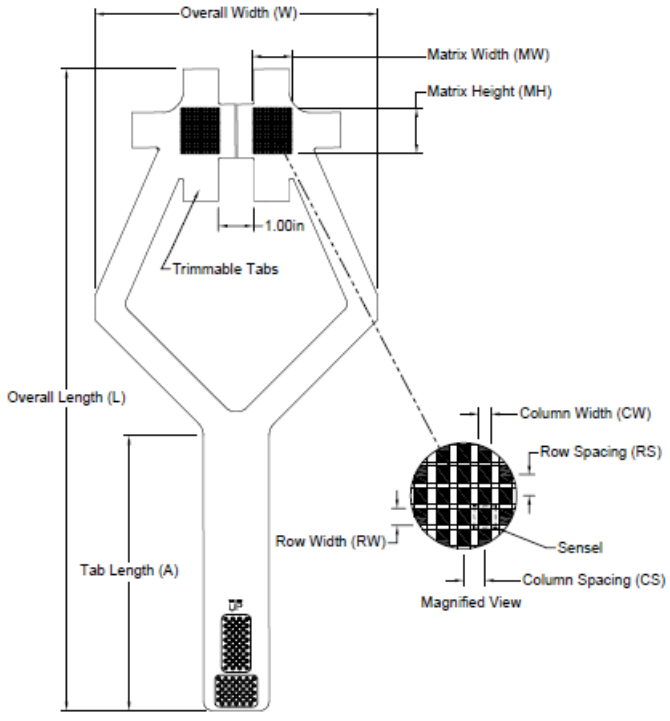

Figure 21: Tekscan Model 4000 pressure mapping sensor [35].

Table 5: Tekscan Model 4000 pressure mapping sensor datasheet [35].

General Dimensions					Sensing Region Dimensions						Summary	
Overall Length *L*	Overall Width *W*	Tab Length *A*	Matrix Width *MW*	Matrix Height *MH*	Columns *CW*	Columns Pitch *CS*	Columns *Qty.*	Rows *RW*	Rows Pitch *RS*	Rows *Qty.*	Total No. of Sensels	Sensel Spatial Resolution
(mm) 462.0	(mm) 203.2	(mm) 198.1	(mm) 27.9	(mm) 33.0	(mm) 0.8	(mm) 1.3	22	(mm) 1.0	(mm) 1.3	26	572	(sensel per sq-cm) 62.0
(in) 18.19	(in) 8.00	(in) 7.80	(in) 1.10	(in) 1.30	(in) 0.030	(in) 0.050	22	(in) 0.040	(in) 0.050	26	572	(sensel per sq-in) 400.0

Pressure Ranges			
kPa	10,343	62,055	68,950
psi	1,500	9,000	10,000

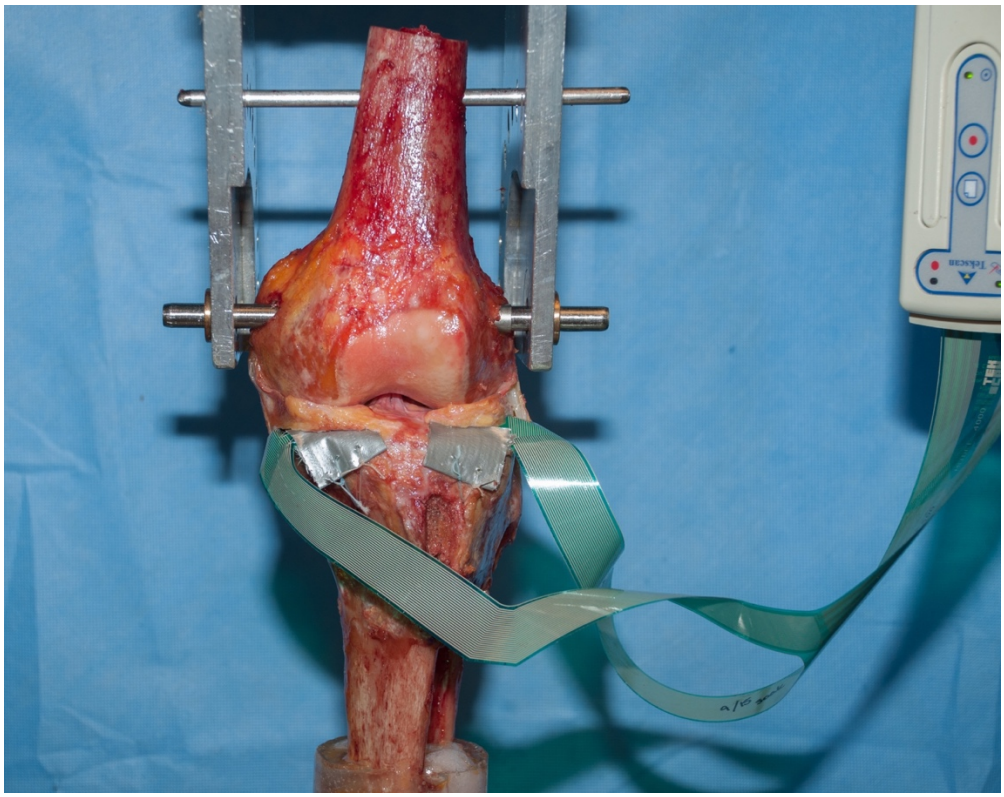

Figure 22: Tekscan sensor instrument placed between menisci and tibial cartilage.

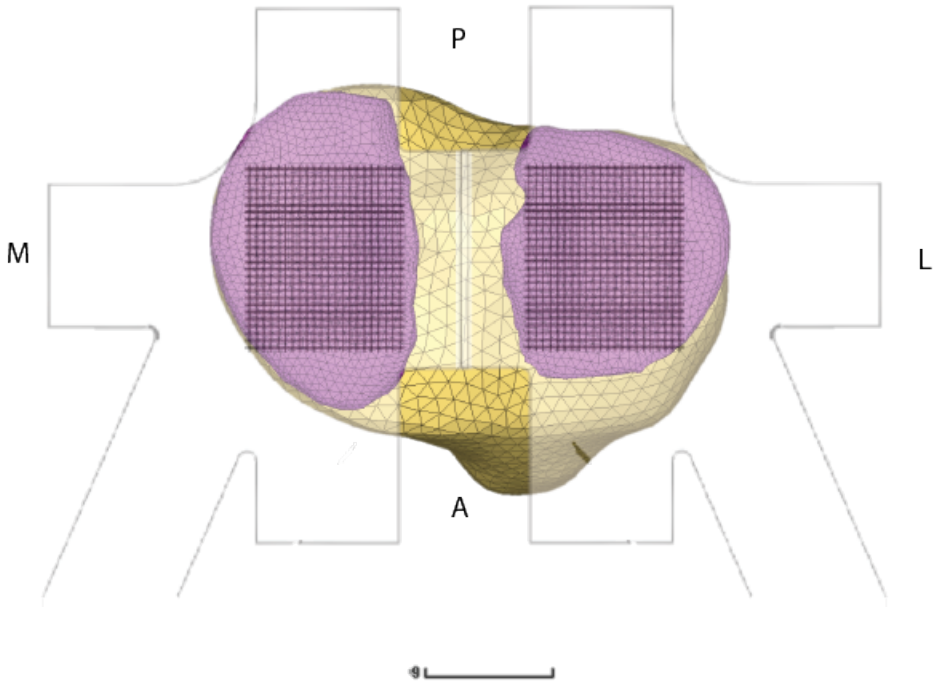

Figure 23: Tekscan sensor footprint on the surface of the tibial cartilages.

3.2 Computational Analysis

The MRI data from a healthy 55-year-old male cadaveric left knee obtained from the Geeslin study was used to develop the three dimensional model in this project. MR imaging is most often used to identify soft tissue and organs from its images, whereas computed tomography (CT) excels in its ability to identify bony constructs more clearly. For the purposes of this project, a combination of MRI and CT scanning could be useful to help differentiate the minute soft tissue anatomy while having the ability to clearly differentiate the bony structures in the knee. While this was unavailable for this study, it is noted as an opportunity for improvement for further patient specific models. Three views from the bare MRI used in this study are shown in Figure 24 below. This knee was noted to have had both MFLs present in the Geeslin study, however upon examination of the MRI scan, the aMFL was not able to be identified and was therefore left out of the model. Often times, it is reported in the literature that identification of the MFLs in MRIs is difficult because of their small cross section and potentially poor contrast in scans. The model was procured from Digital Imaging and Communications in Medicine (DICOM) files using manual segmentation in 3D Slicer open source software [37]. Segmentation, as mentioned before, is a term that is used to differentiate each anatomical volume in the modeling software. This is done in the software by creating voxels, or a set of 3D arrays instead of 2D pixels on the images. MRI scans which offer the axial, sagittal, and coronal sliced images, create the voxels through stitching together each view. Figure 25 shows outlines of each component in the three views of the MRI. After all of the necessary anatomy was traced in the model, the 3D view of the knee was created, as seen in Figure 26 and Figure 27.

A) B) C)

Figure 24: MRI slices were used to create a 3D model. A) Axial view, B) sagittal view, C) coronal view.

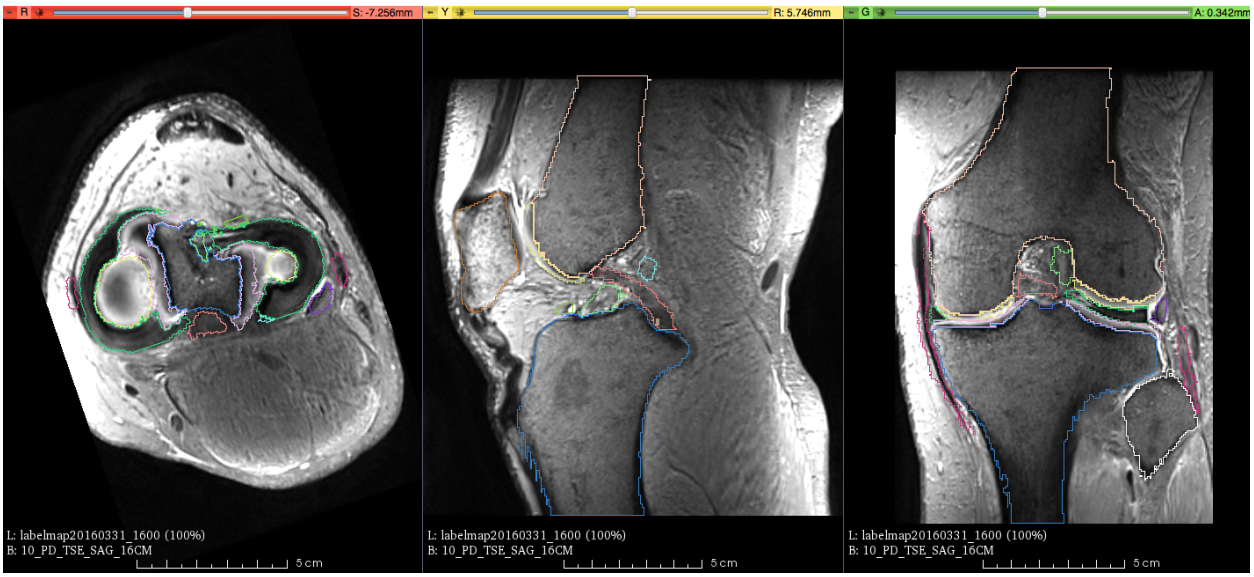

A) B) C)

Figure 25: Outline of each volume are represented by different colors. The A) axial view, B) sagittal view, and C) coronal view.

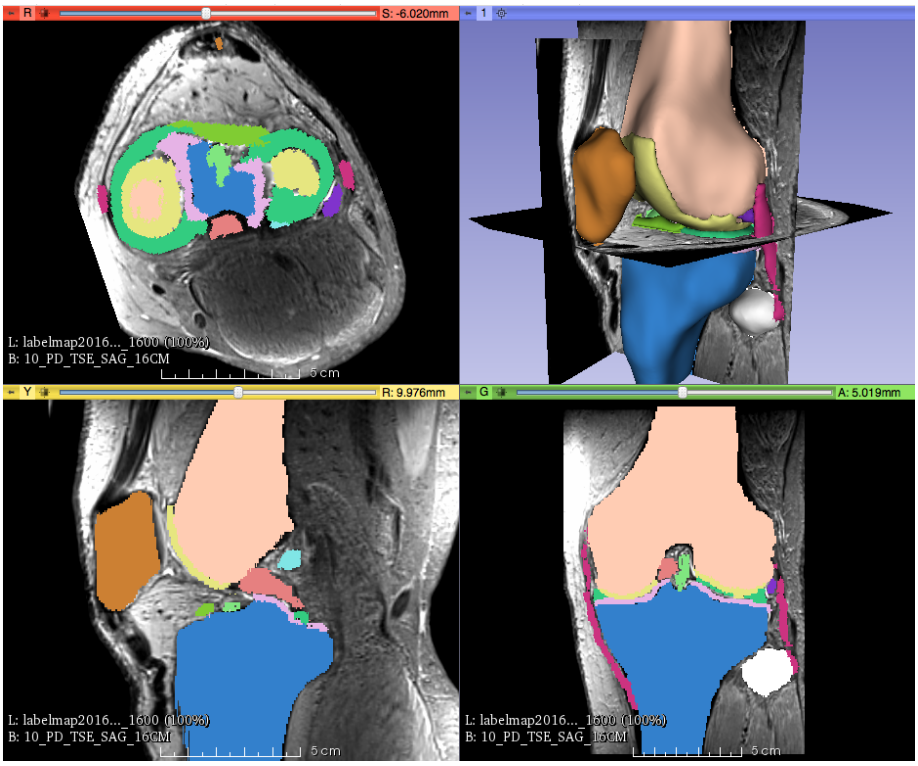

Figure 26: Voxels from each slice align to create the 3D model of the knee.

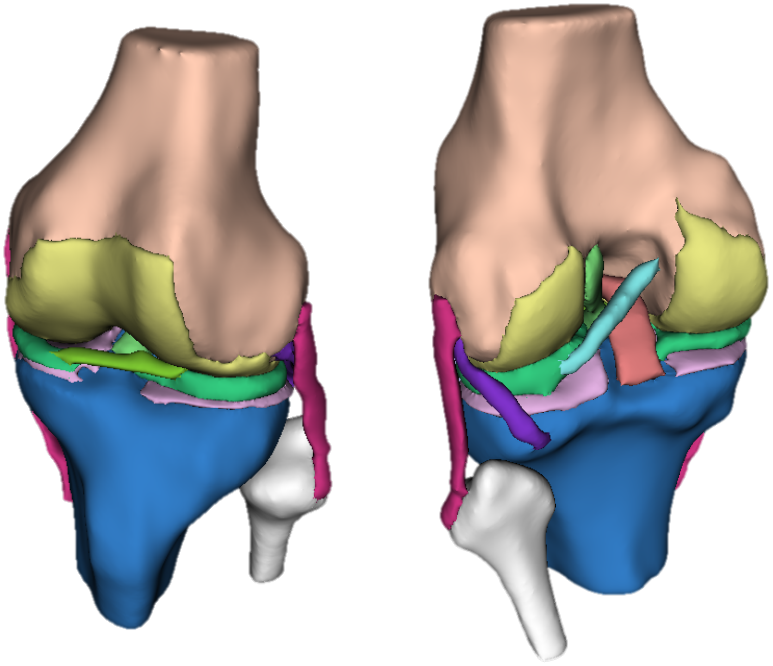

Figure 27: 3D model generated from segmentation using 3D Slicer. Anterior and posterior views.

Once each anatomical structure of interest was harvested from the MRI, the model was able to be extracted into 3D surfaces. Several smoothing operations were necessary in order to remove the poor resolution regions. Because of the resolution of the MRI slices, the initially procured data proved to be rough. Smoothing was initially done inside of the 3D Slicer software as well as in meshing softwares MeshLab [38] and HyperMesh [39] This was done by initially exporting the created surfaces using stereolithography (.stl) files, or triangulated surfaces, to MeshLab software. Each smoothing operation with run the structures through multiple smoothing algorithms in the software to produce more idealize surfaces. These smoothed surfaces will in turn produce more desirable results during solving which will be easier for the solver to work with. For example, Figure 28 clearly shows how smoothing operations can significantly improve the models outcome.

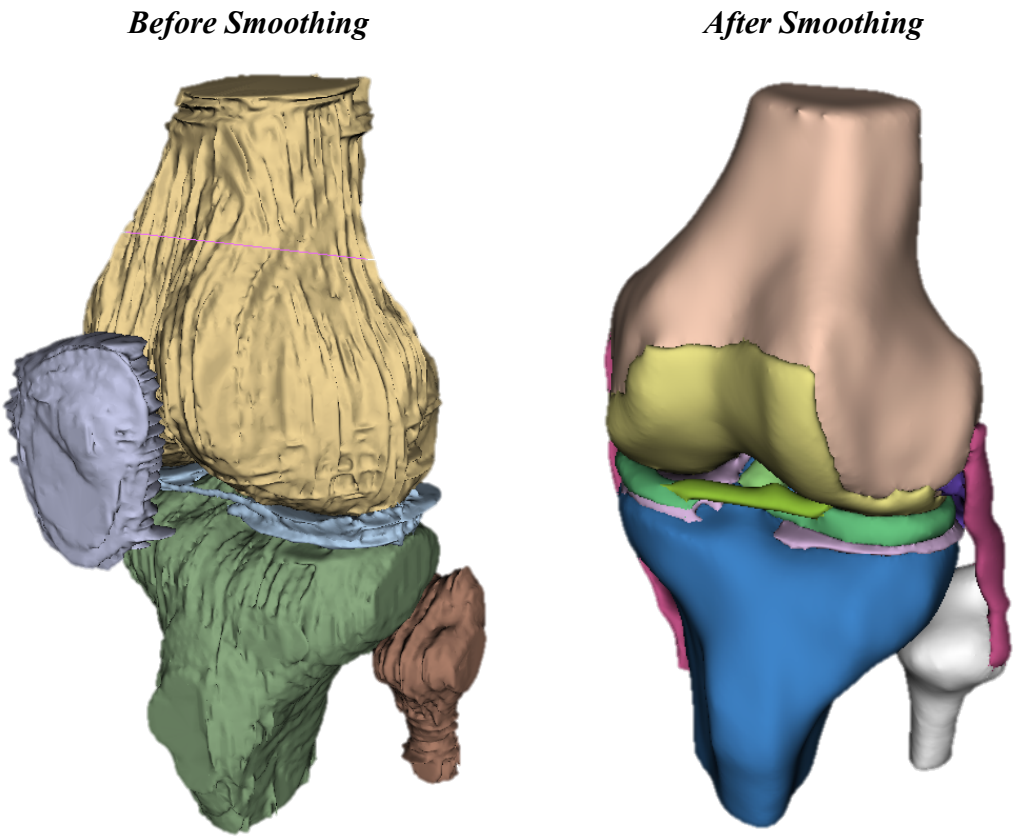

Figure 28: An example of how significantly improved the model can become through smoothing operations using Meshlab and HyperMesh (LCL/MCL not included in unsmoothed model, patella not included in smoothed model).

After smoothing in MeshLab, the components were exported into HyperMesh for further pre-processing. HyperMesh was chosen because it has the ability to interface with many FE solvers by creating a unique input file that a large range of solvers can support. For the purposes of this study, HyperMesh used its Abaqus user profile, which is highly compatible with Calculix, as its FE solver. Calculix was used as the main solver for this work.

It is important to note the model's anatomical accuracy was verified throughout the development process of the study by the co-authors'. Validation of the model's root insertion points are shown in Figure 29. Root insertions and ligament footprints align with great agreement from A) in the cadaver image to B) with the model image. Additionally, placement of the pMFL on the lateral meniscus is shown in Figure 30. Overall, the model checks out for good anatomical agreement. This is to be expected because the model itself came directly from MRI of the cadaver knee. However, it was still important to put in places these checks to ensure the smoothing did not remove any important structures in the knee.

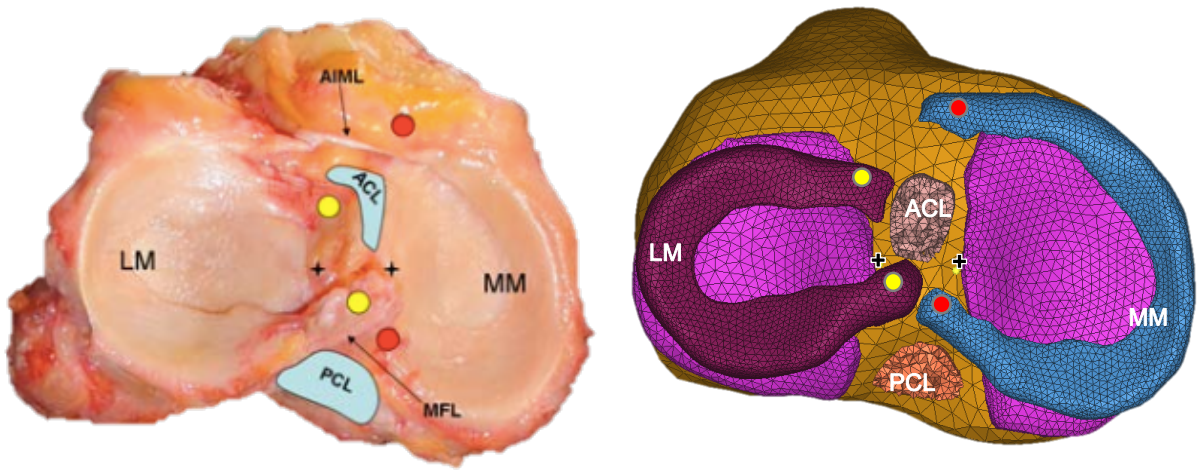

A) B)

Figure 29: Axial view of the knee. A) Cadaver image from [11], B) 3D model. Medial attachments of roots (red dots); Lateral attachments of roots (yellow dots). Black starts: apex of medial and lateral intercondylar eminence. LM, lateral meniscus; MM, medial meniscus; ACL, anterior cruciate ligament; PCL, posterior cruciate ligament; AIML, anterior intermeniscal ligament (not pictured in B); MFL meniscofemoral ligament (not pictured in B).

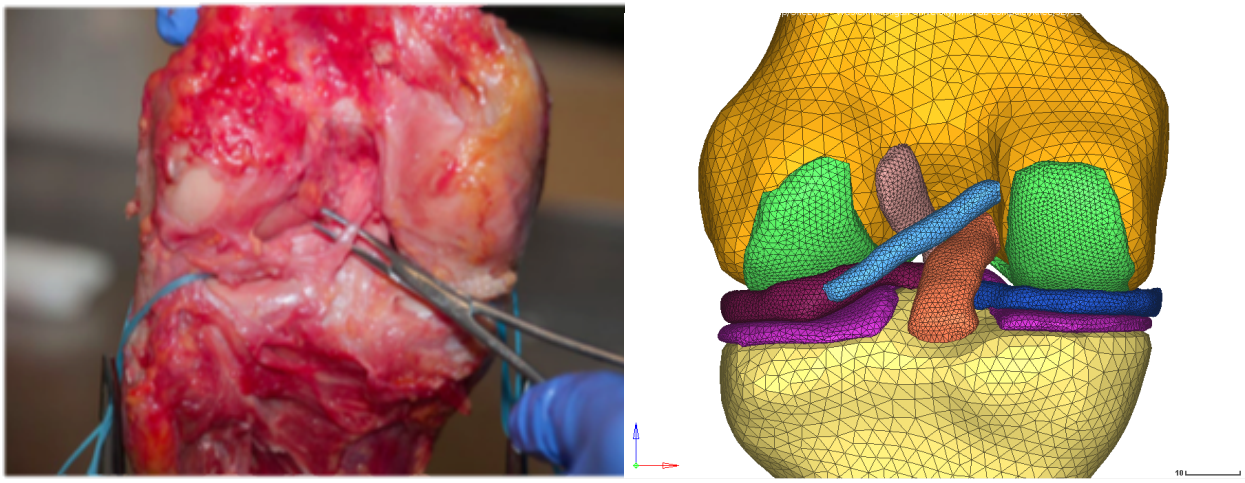

Figure 30: Posterior view of A) cadaver image from [17], B) 3D model showing placement of pMFL on lateral meniscus and its insertion into the femur.

The full components of the model differed only slightly from that of the anatomy specifically used in the study done by the Geeslin study. That is, the fibula, popliteus tendon, medial collateral ligament (MCL), and lateral collateral ligament (LCL) were excluded in order to simplify the model further. Their removal was justified both by the co-author's agreement and for the purposes of the study observing only at 0° flexion. The medial and lateral meniscus, anterior cruciate ligament (ACL), posterior cruciate ligament (PCL), pMFL (aMFL not included due to poor resolution on DICOM), and articular cartilage of the femur and tibia were all included in the model. The skin, subcutaneous tissue, muscles, tendons, central aspect of the posterior capsule, and patella were not included in the model, which is consistent with what was done in the study by the Geeslin study.

3.2.1 Material Properties

10-noded, quadratic tetrahedral elements were used for all ligaments and soft tissue. Bones were treated as rigid bodies due to their negligible effects to the overall solution and to allow for a computational cost savings for the problem, which is consistent with the literature [21 22 25]. Material properties used for the model were based on the literature as well. Articular cartilages were treated as linear elastic, isotropic. Menisci were transversely isotropic linear elastic and material properties were applied to a local cylindrical coordinate system which was user defined.

Menisci roots were assumed to be the same as the menisci, and therefore not treated differently. Ligaments were treated as hyperelastic, Neo-Hookean materials. A summary of the material properties used can be seen in Table 6. The final meshed model can be seen in Figure 32 and Figure 32. An element size of 1 mm was used for the ligaments. Cartilages were made to be 1 mm near the contact regions, but gradually increased to 2.5 mm in non-contact regions. Menisci were also made to be 1 mm element sizes. Using HyperMesh, nodes, elements, and surfaces can be generated to the main input file where further modifications can be made. Element counts for each component is listed in Table 7.

Table 6: Material Properties used for model components.

Femur/Tibia	Rigid Body	N/A	[21 22 25]
Femoral/Tibial Cartilage	Linear Elastic Isotropic	E = 15.0 MPa ν =.475	[21 22 24]
Medial/Lateral Meniscus	Linear Elastic Transversely Isotropic	E_1 = 20 MPa (radial) E_2 = 120 MPa (circumferential) E_3 = 20 MPa (axial) ν_{12} = 0.3 ν_{13} = 0.2 ν_{23} = 0.3 $G_{12} = G_{13}$ = 57.7 MPa G_{23} = 8.33 MPa	[23]
ACL	Hyperelastic Neo-Hookean	C_{10} = 1.95 D = 0.0068	[22 25]
PCL/pMFL	Hyperelastic Neo-Hookean	C_{10} = 3.25 D = 0.0041	[22 25]

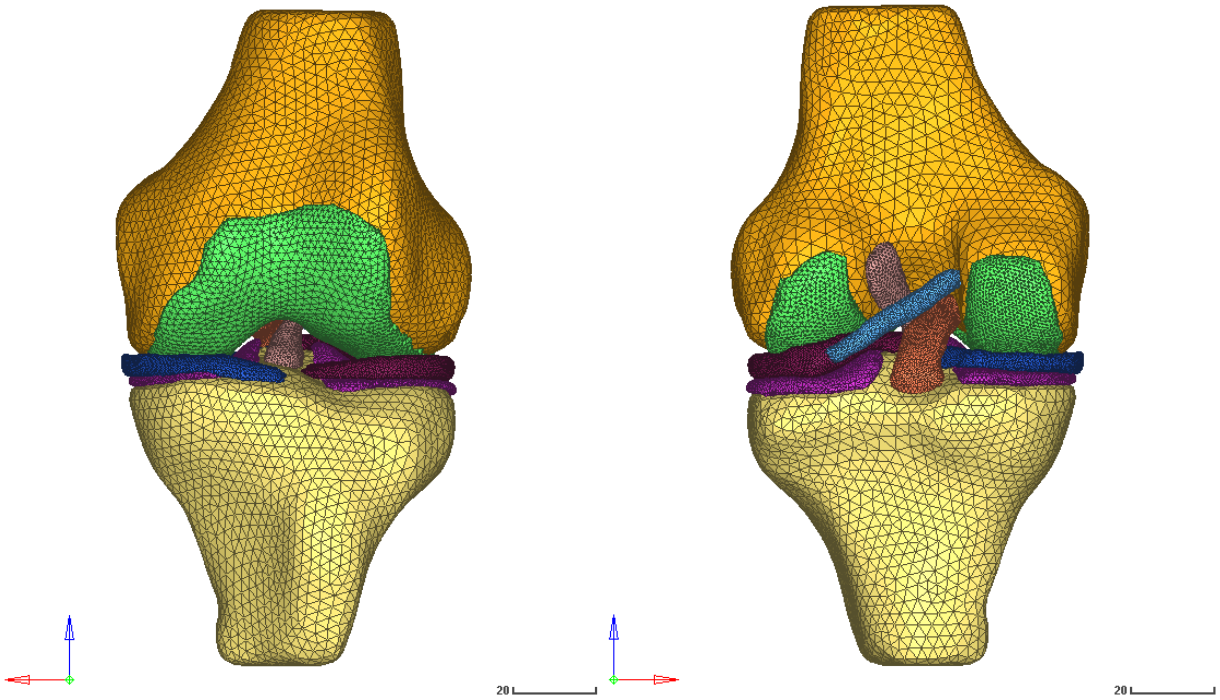

Figure 31: Meshed 3D model of the knee – anterior and posterior views.

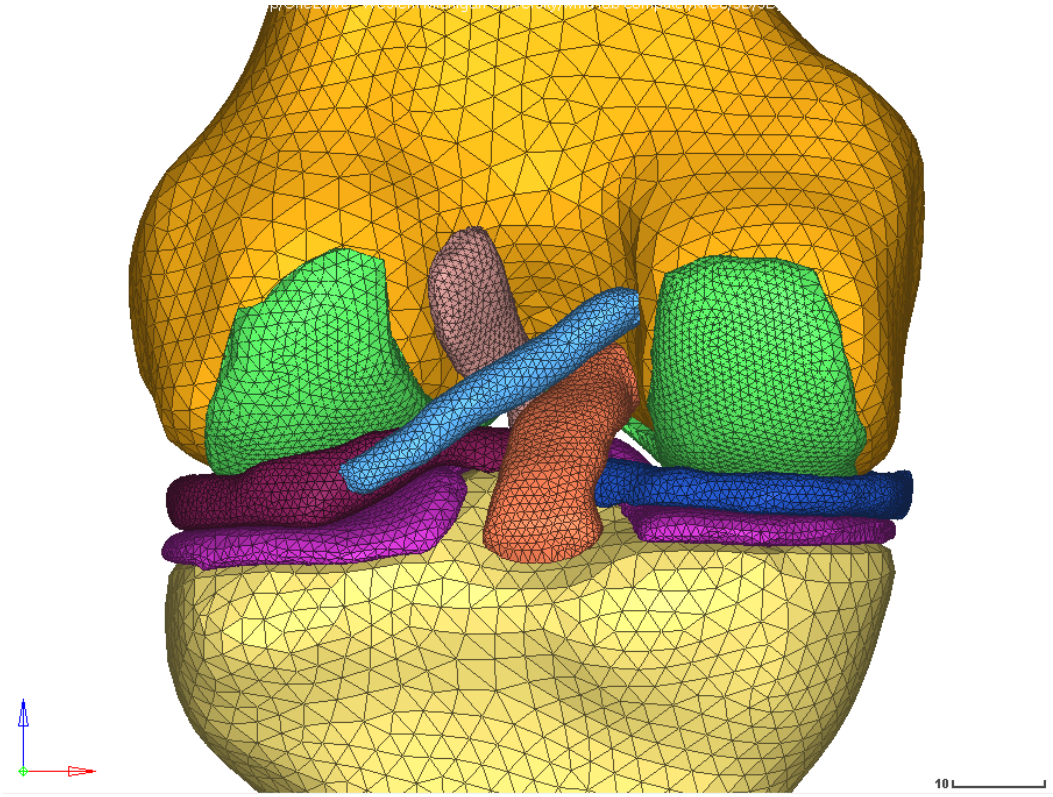

Figure 32: Meshed 3D model of the knee – posterior view.

Table 7: Elements per component.

Component	*PCL*	*ACL*	*pMFL*	*Femoral Art. Cartilage*	*Tibial Art. Cartilage*	*Lateral Meniscus*	*Medial Meniscus*
Elements	8,714	8,140	4,426	21,696	13,500	15,318	11,103

3.2.2 Boundary Conditions

The femur was fixed in five degrees of freedom, allowing for z-axis translation to accommodate for the applied load, as done in the experimental study done by Geeslin et al. The tibia was fixed in all translational degrees of freedom and all but the Y rotational degree of freedom. This was done even though the experimental setup allowed for freedom of X and Y translation as well as rotation in the X and Z. This choice was made for two reasons. Constraining all translational degrees of freedom ensured there was no rigid body motion in the model would exist. This decision was also made because the effects of the ACL were not to be monitored in the model, as mentioned previously. Additionally, the Y axis (varus/valgus axis) was given freedom to rotate to allow the model to balance the load distribution as a normal knee would in load. This operation was done in the experimental setup before constraining with the fixturing – that is, equal loading was ensured in both compartments prior to the test load was applied. Because there was limited ability to do this properly in the model, this methodology to the applying the boundary conditions allowed for this type of balancing to occur.

The model was axially loaded in compression at 1,000 N at a flexion angle of 0°. This compressive load replicated that used in the Geeslin study and the flexion angle corresponds to full extension of the knee joint. The load, which is nearly the weight of a normal male, is widely used in the literature, both experimentally and computationally [14 17 22]. The model boundary conditions applied are shown visually in Figure 33.

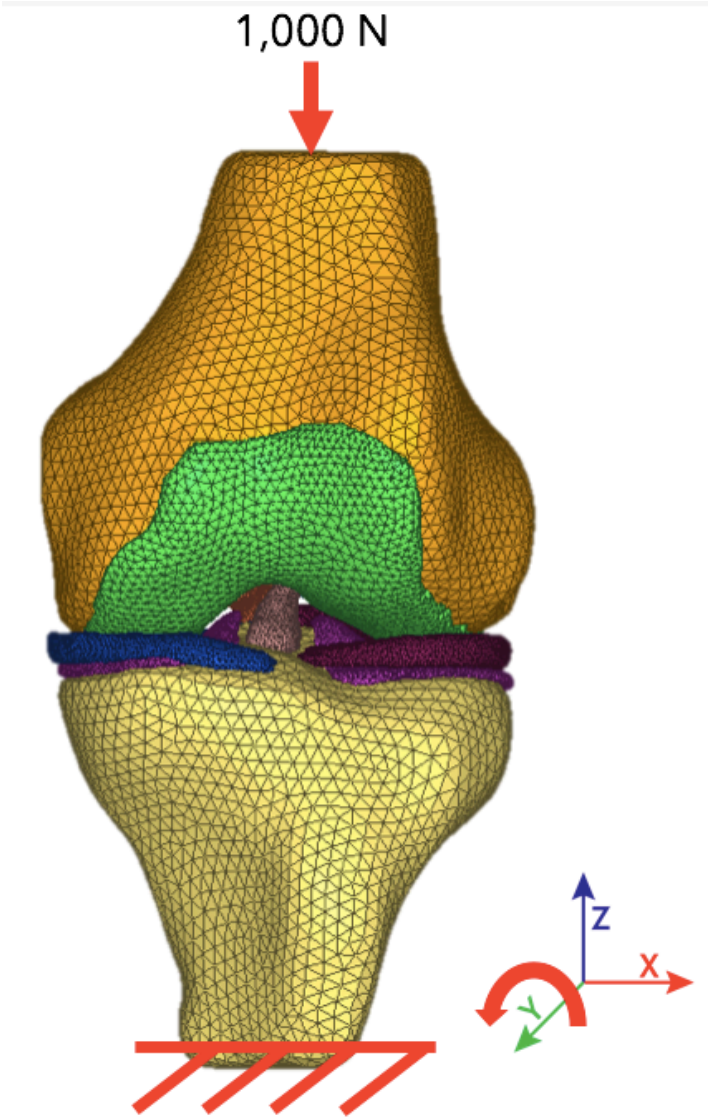

Figure 33: Boundary conditions applied to model.

Contact was modeled using the linear pressure-overclosure relationship because of its lower computational cost and therefore higher likelihood to reach convergence. Constant parameter *K* was set to 75 N/mm^3 for all contact pairs which were free to move about each other. Friction was neglected between articular surfaces of the tibia and femur to simulate frictionless contact. Ligament insertions into bone were modeled using tied contact. This effectively means that the dependent, or slave, surfaces within a certain range of the independent, or master, surfaces will become bonded. This was also used for the meniscus root insertions and the bonding of the cartilages on the surfaces of the bone.

As mentioned before, the focus of this work is to simulate three conditions: (1) intact, (2) LMPRA, (3) LMPRA and deficient MFLs. Three different finite element models were created to reflect these first three conditions done in the experiment done in the Geeslin study, which this work is an extension of. LMPRA will be modeled by removing the insertion point of the meniscus root to the tibial plateau. Deficient MFLs will simply be modeled by removing the MFL component from the model.

The input files for conditions 1, 2 and 3 are located in Appendices A, B, and C, respectively.

CHAPTER 4 RESULTS

4.1 Contact Area

For a 1,000 N compressive load at 0° flexion, the FEA yielded agreeable results for both the lateral and medial compartments of the knee. For condition 1 in the lateral compartment, contact area on the tibial cartilage was determined to be 446 mm^2. Contact area for condition 2 was 356 mm^2. In contrast to the Geeslin study which concluded from the experimental work that conditions 2 did not present a significantly different result compared to the intact condition, there was a noticeable difference in contact area for the computational results. Condition 3 provided contact area results of 310 mm^2. Lateral compartment results from conditions 1, 2, and 3 for contact area are compiled in Table 8 for comparison against the experimental data. A percent difference between studies is also detailed in the table. While not discussed in the Geeslin study, contact area results and comparative values for the medial compartment are located in Table 9. Additionally, bar graphs showing the comparison between experimental and computational results are show in Figure 34 for contact area the lateral compartment. Contact area for the medial compartment is shown in Figure 35.

The measurement of contact area was determined based on whether contact pressure was detected on the surface of the tibial cartilage. This was the approach to the experimental data processing as well as for the computational. Because Calculix lacks the ability to interpret contact area directly, an additional post processing step was necessary. This was done by using an image to value algorithm that reads an image's pixel color and assigns a number to the pixel. If the color associated with contact was detected, that pixel area was flagged to be in contact and therefore added to the total contact area being calculated. It would be advantageous for Calculix to provide a much simpler method to count elements on a surface that are in contact.

Table 8: Results for lateral compartment contact area [mm^2].

CONTACT AREA [mm^2]	**Condition**		
	1	2	3
Experimental	516	521	303
Computational	446	356	310
%Δ	-14%	-32%	2%

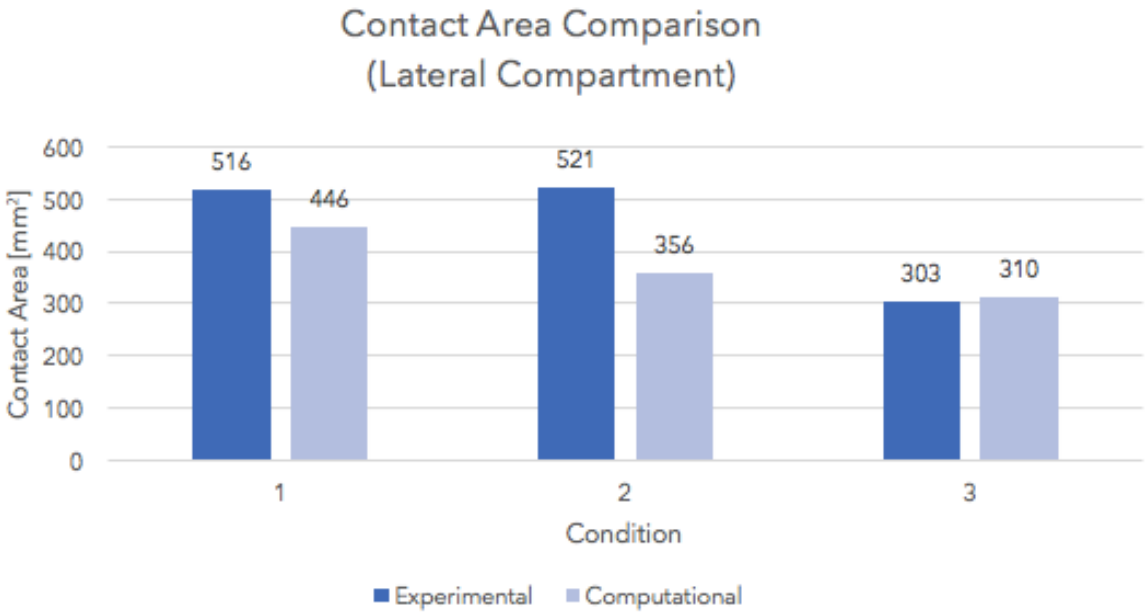

Figure 34: Experimental vs. Computational results for lateral compartment contact area [mm^2].

Table 9: Results for medial compartment contact area [mm^2].

CONTACT AREA [mm^2]	**Condition**		
	1	2	3
Experimental	611	635	627
Computational	467	404	428
%Δ	-24%	-36%	-32%

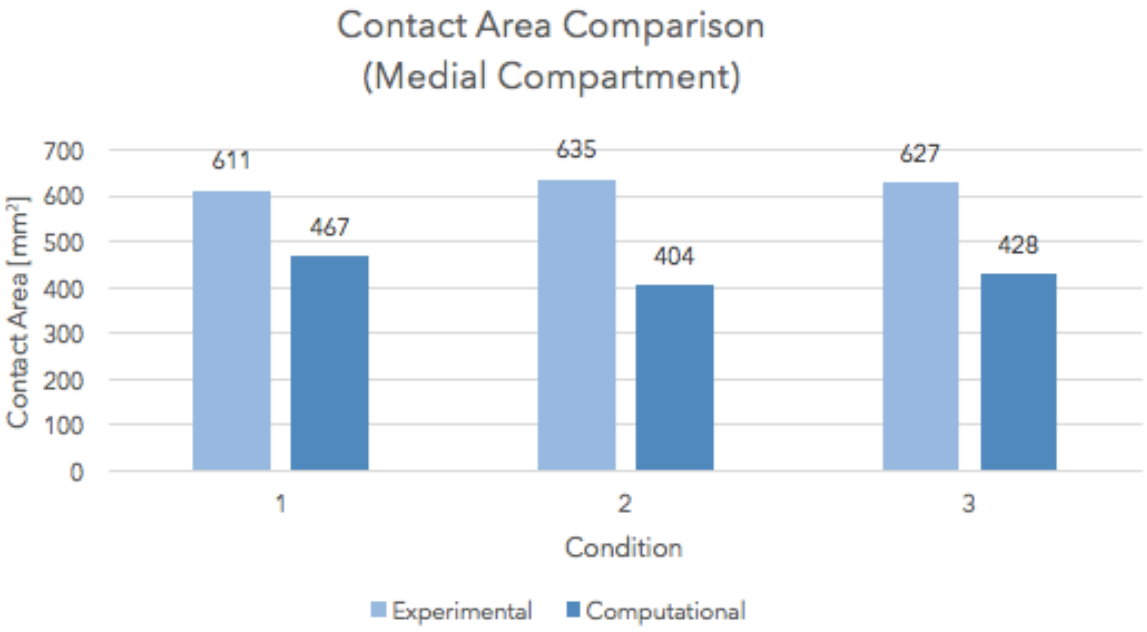

Figure 35: Experimental vs. Computational results for medial compartment contact area [mm^2].

4.2 Peak Pressure

Condition 1 produced a peak contact pressure of 2.84 MPa. Peak contact pressure for condition 2 was 2.89 MPa. The computational results agree with the Geeslin study where these values did not present a significantly different result compared to that from the intact condition. Condition 3 provided a peak pressure value of 2.98 MPa. Lateral compartment results from conditions 1, 2, and 3 for are compiled in Table 10 for comparison against those from the experimental data with percent difference between studies included. Peak contact pressure results and comparative values for the medial compartment are located in Table 11. Additionally, a bar graph showing the comparison between experimental and computational results are show in Figure 36 for peak contact pressure in the lateral compartment and in Figure 37 for the medial compartment.

Contour plots of each condition were generated from the experimental data and computational analyses. Plots were scaled and colored accordingly to allow for ease of interpretation across both datasets, even though different programs were used to process the data (Tekscan was the instrumentation used to measure the experimental data and Calculix was used to solve and post process the computational model). Each plot also gives coordinates of the anatomy – lateral, medial, anterior, posterior. The views should be interpreted as a top down, axial view of the tibial cartilage of both the lateral and medial compartments of the knee. Figure 38 and Figure 39 show the contact pressure contour plots for condition 1 – intact knee – for the experimental and computational analysis, respectively. Figure 40 and Figure 41 showcase the contact pressure results for condition 2 – LMPRA – for experimental and computational analyses, respectively. Lastly, Figure 42 and Figure 43 show the contact pressure results for condition 3 – LMPRA with deficient MFL, for experimental and computational analyses, respectively.

Table 10: Results for lateral compartment peak contact pressure [MPa].

PEAK PRESSURE [MPa]	**Condition**		
	1	2	3
Experimental	3.63	3.30	4.62
Computational	2.84	2.89	2.98
%Δ	-22%	-12%	-35%

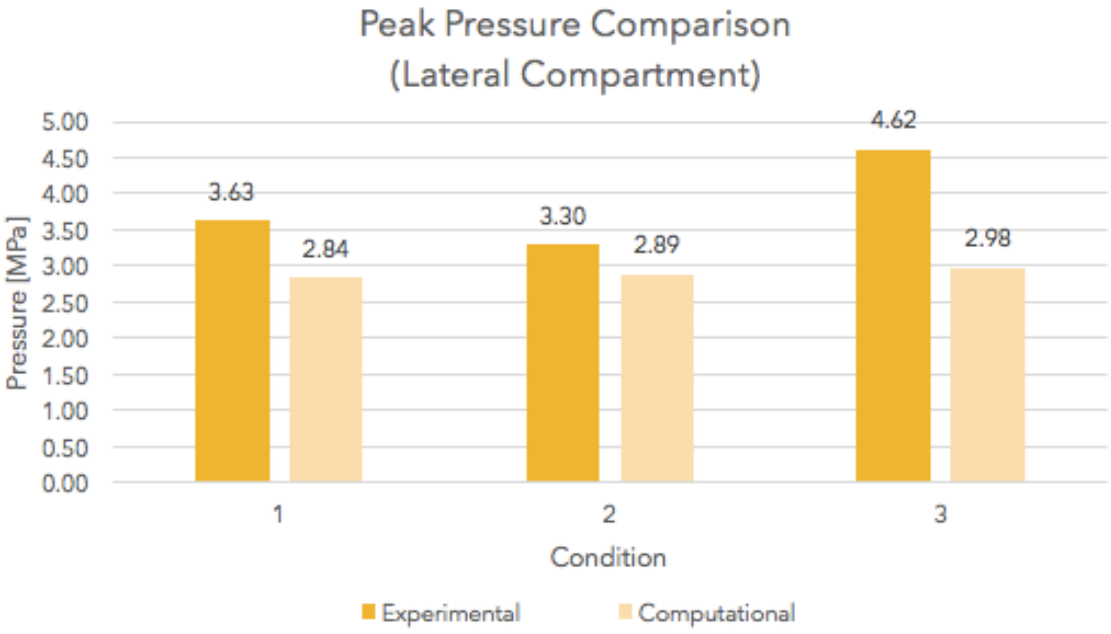

Figure 36: Experimental vs. Computational results for lateral compartment peak contact pressure [MPa].

Table 11: Results for medial compartment peak contact pressure [MPa] at 0° flexion.

PEAK PRESSURE [MPa]	**Condition**		
	1	2	3
Experimental	2.45	2.45	2.07
Computational	3.03	3.06	3.08
%Δ	24%	25%	49%

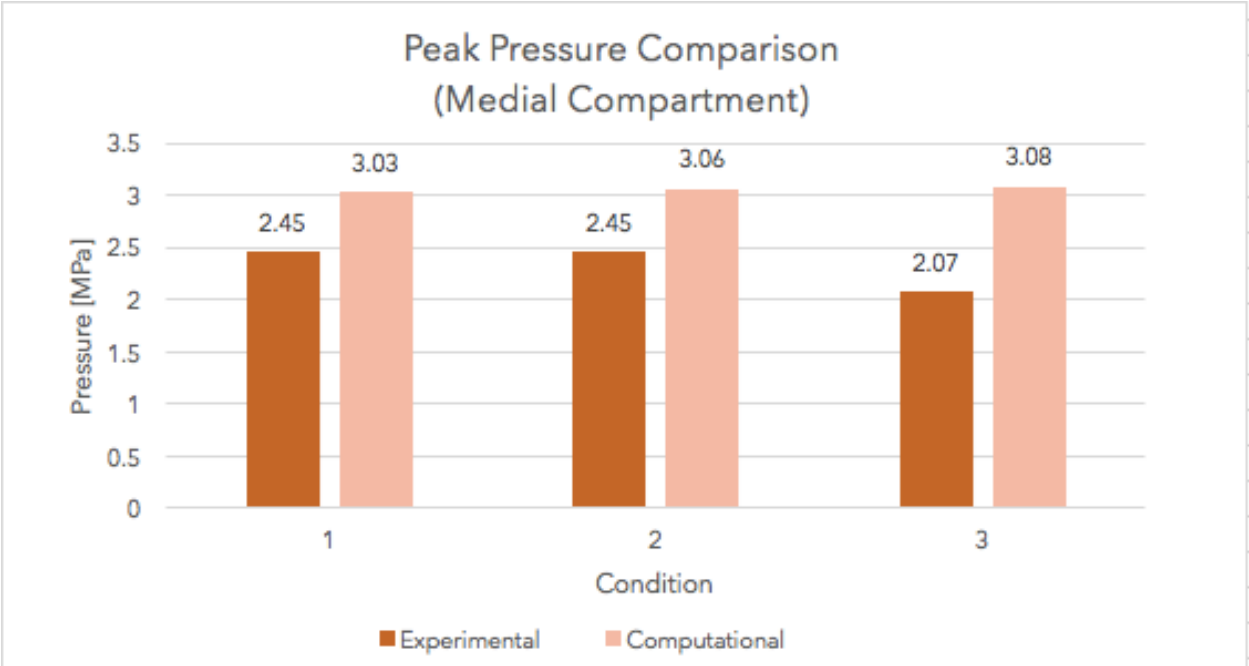

Figure 37: Experimental vs. Computational results for medial compartment peak contact pressure [MPa].

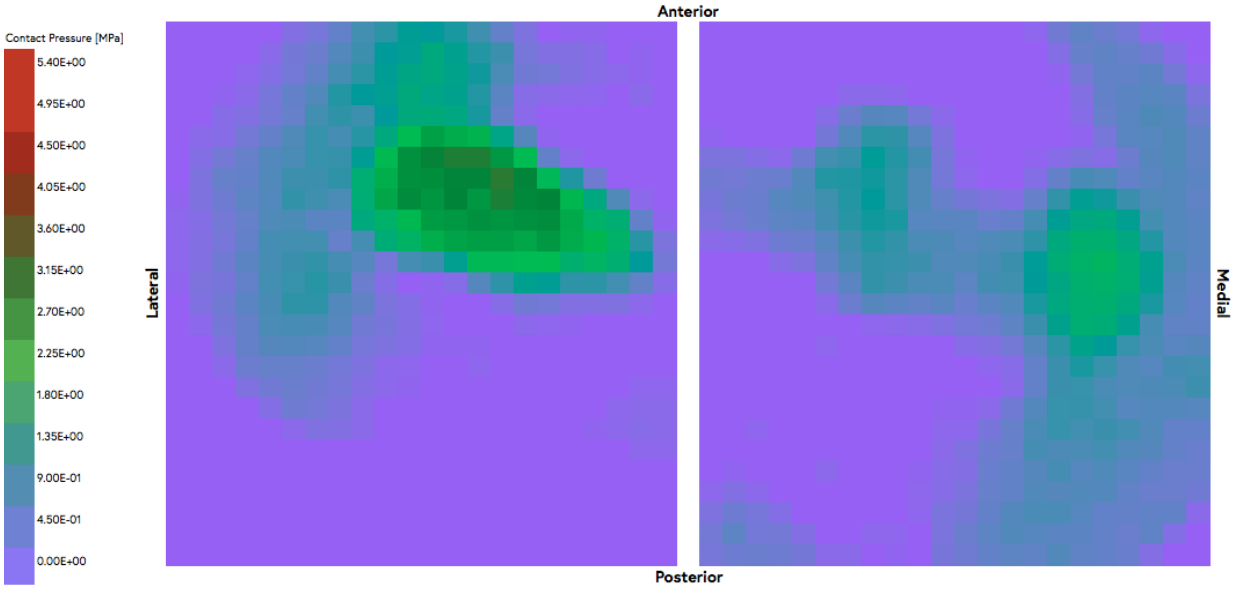

Figure 38: Condition 1 – Intact, Experimental contact pressure contour (left = lateral compartment, right = medial compartment).

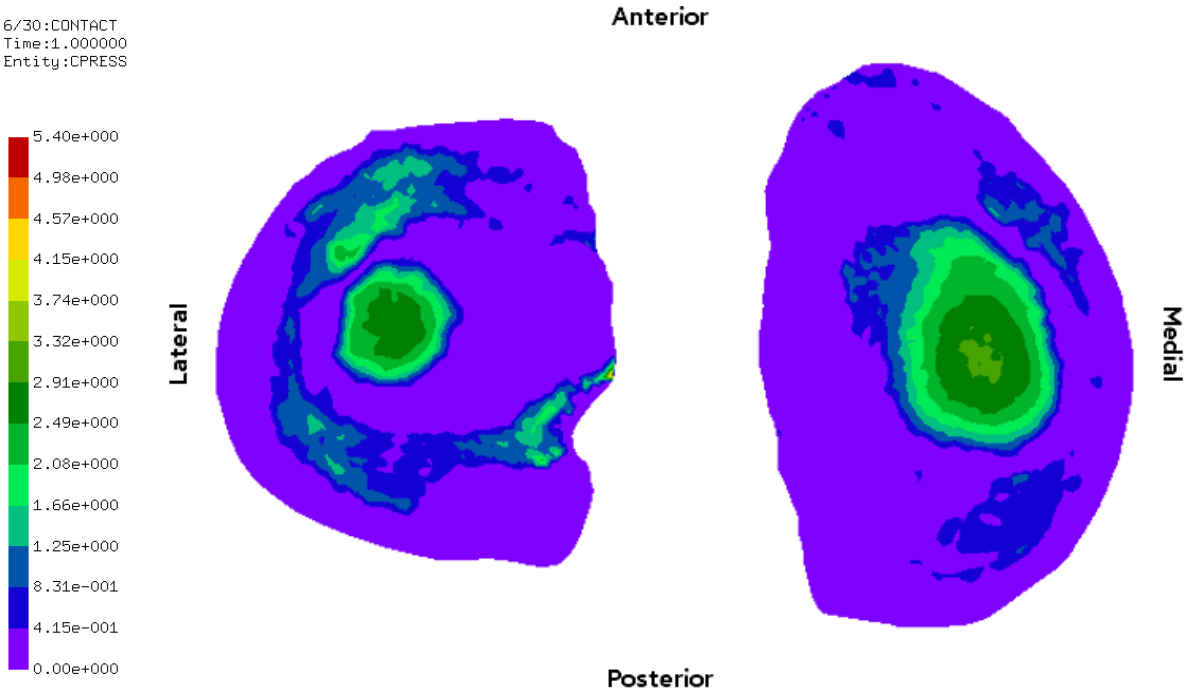

Figure 39: Condition 1 – Intact, Computational contact pressure contour (left = lateral compartment, right = medial compartment).

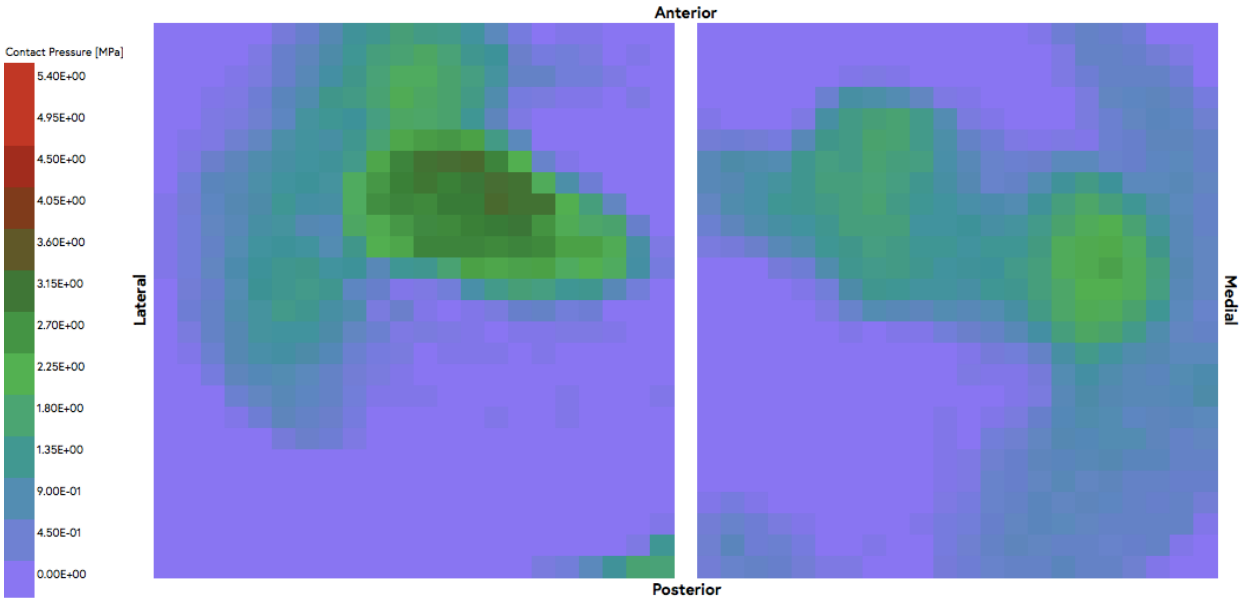

Figure 40: Condition 2 - LMPRA, Experimental contact pressure contour (left = lateral compartment, right = medial compartment).

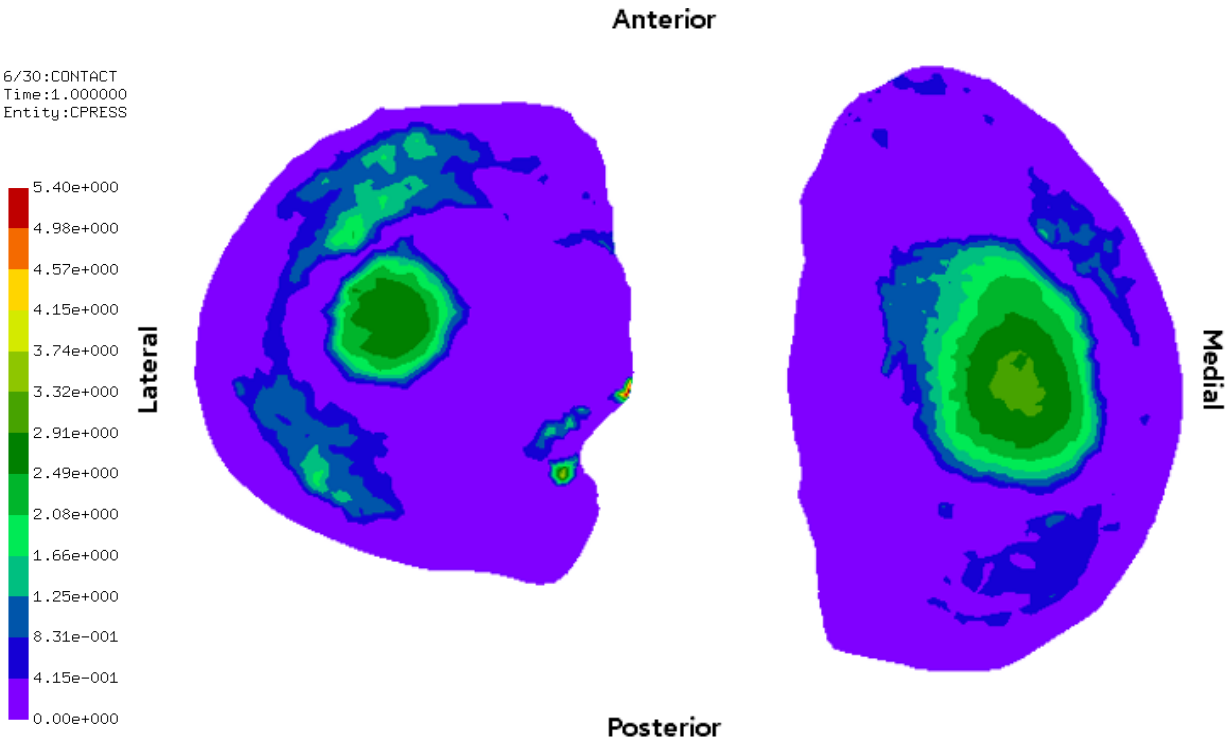

Figure 41: Condition 2 - LMPRA, Computational contact pressure contour (left = lateral compartment, right = medial compartment).

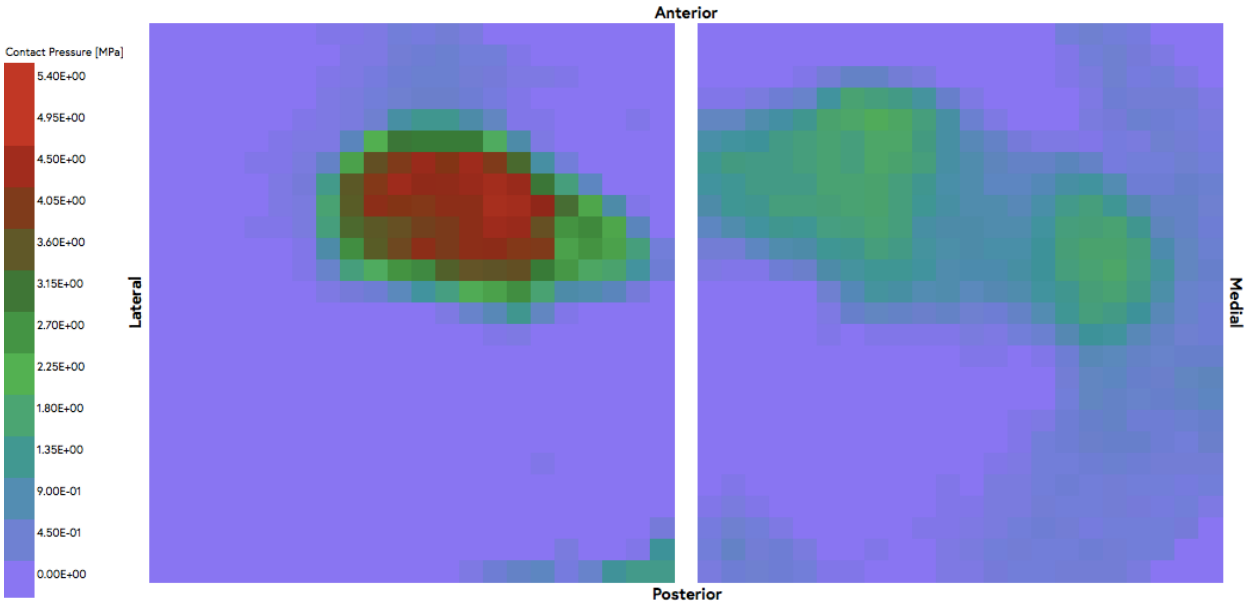

Figure 42: Condition 3 - LMPRA with Deficient MFL, Experimental contact pressure contour (left = lateral compartment, right = medial compartment).

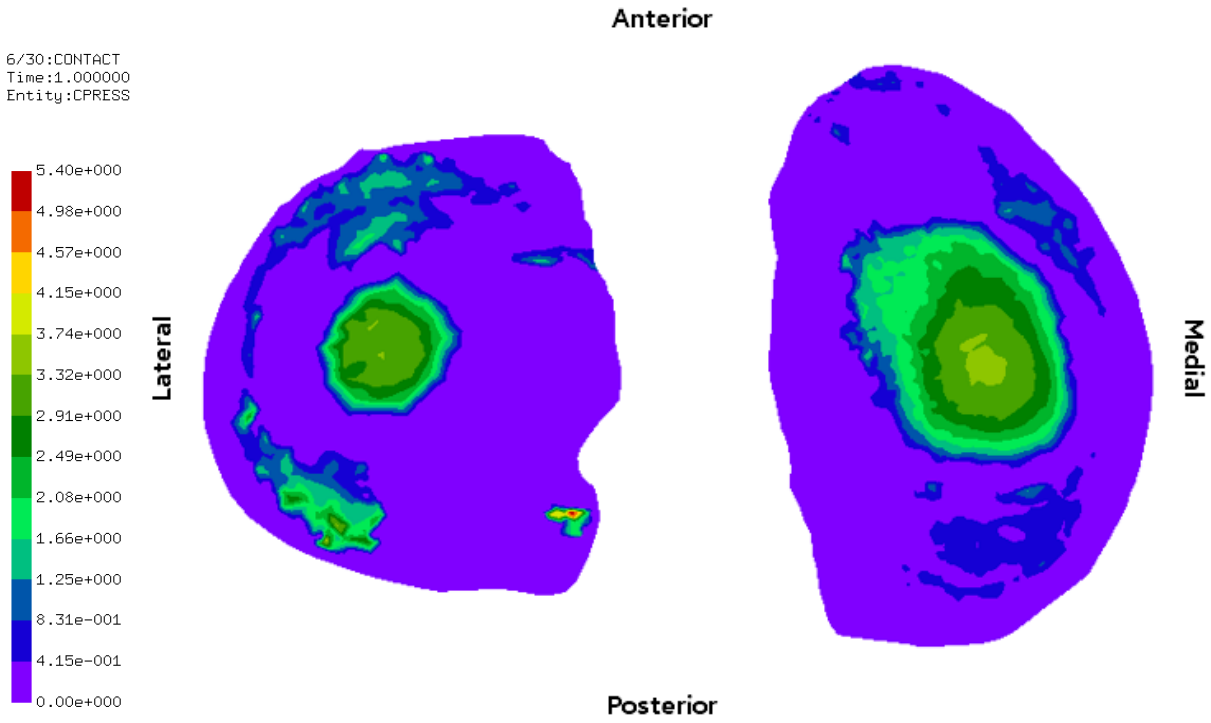

Figure 43: Condition 3 - LMPRA with Deficient MFL, Computational contact pressure contour (left = lateral compartment, right = medial compartment).

4.3 Stress Analysis

While not directly studied in the Geeslin study due to experimental limitations, the ability to observe stresses in the pMFL was collected for conditions 1 and 2 with the computational results. Stress distribution in the pMFL in the form of Von Mises stress is shown in Figure 44 for both conditions 1 and 2.

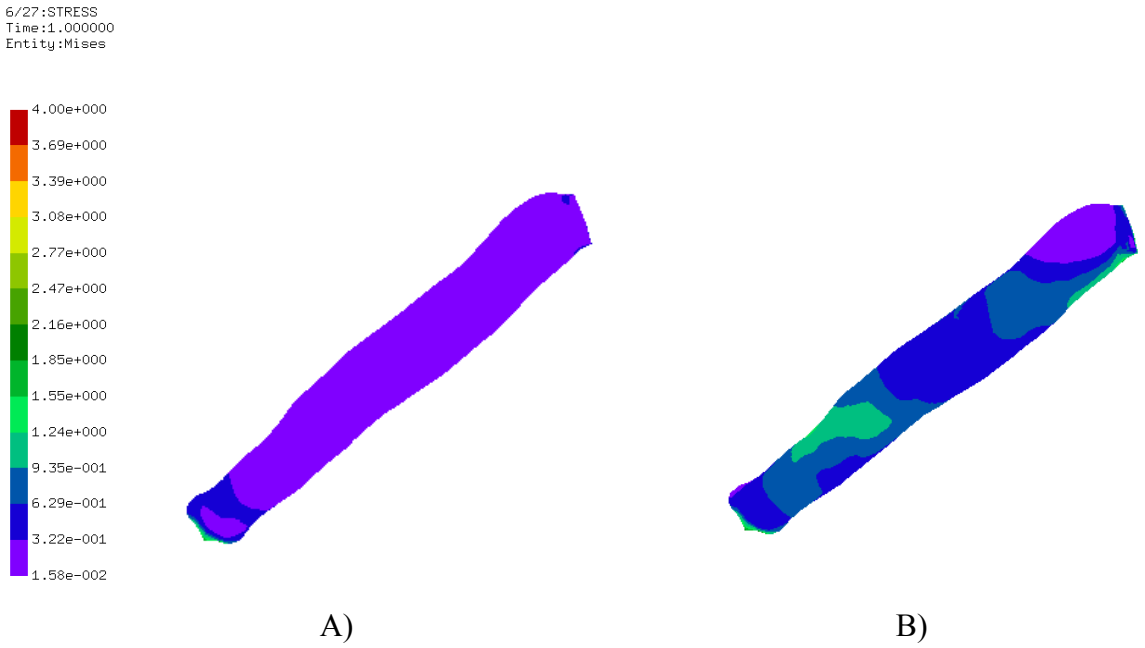

Figure 44: Stress distribution (Von Mises) of the pMFL for A) Condition 1 – Intact and B) Condition 2 - LMPRA.

Additionally, stress distribution in the lateral and medial menisci can be seen in Appendix D for all 3 conditions.

CHAPTER 5 DISCUSSION

The largest discrepancies in comparative results stemmed from condition 3 for contact area in the lateral (35%) and medial (49%) compartments and for condition 2 for peak pressure in the lateral (32%) and medial (36%) compartments. Even so, the results still were on trend and within an acceptable range of variability to the experimental results. The known trend for each condition is that for condition 1, intact, comparted to condition 2, LMPRA – little to no change in contact mechanics is present for 0° flexion. While the experimental results were not exact to this, the deviation is deemed within an acceptable range. In contrast, from condition 1 to condition 3 – LMPRA and deficient MFLs – an inverse relationship appears from contact area to peak pressure. That is, contact area will begin to decrease and peak pressure will increase. This was true in the Geeslin study as well as for others in the literature [14 17 22]. The computational results, while not producing as clear of a trend as the experimental results, did show a decrease in contact area from conditions 1 and 2 to 3 (446 mm^2, 356 mm^2, 310 mm^2, respectively) as well as an increase in peak contact pressure from conditions 1 and 2 to 3 (2.84 MPa, 2.89 MPa, 2.98 MPa, respectively). This in itself proves that the model produces a valid result, even if the direct comparison to the experimental data is not exact.

It was noted during development that the medial meniscus showed signs of deterioration and thinning both in the model and cadaver specimen, shown in Figure 45. That, in addition to analyzing the medial compartment results, provide suspicion as to whether this had an impact on the lateral compartment results. It can be seen in the contact pressure distributions that nearly no residual contact from the medial meniscus is shown. This could be a contributing factor to the resulting values in the lateral compartment. Additionally, the medial meniscus showed signs of extrusion prior to any loading which may add to this altered biomechanical contact responses. This is shown in Figure 46. Other physical differences in the model could stem from the experimental model having the presence of both aMFL and pMFL whereas the computational

model only had the pMFL. This too could have resulted in the differences in contact area and pressures from the experimental values.

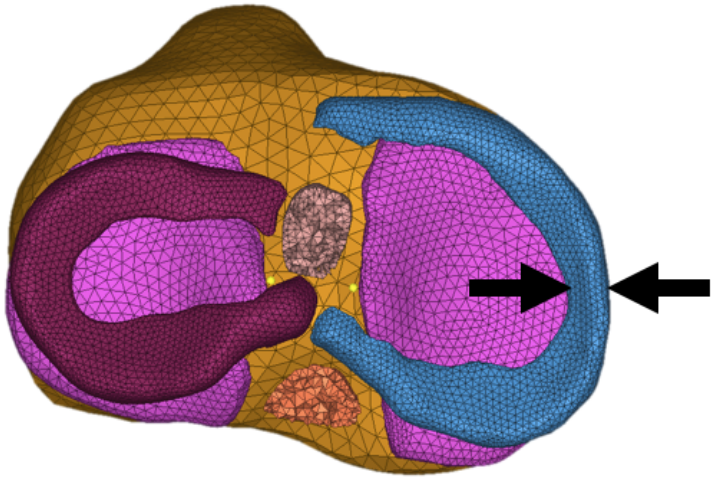

Figure 45: The medial meniscus shows signs of thinning medially, potentially altering biomechanical contact responses in both the lateral and medial compartments.

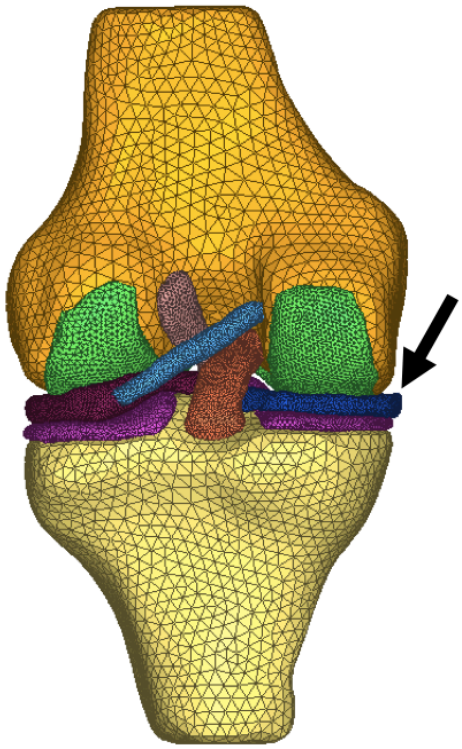

Figure 46: The medial meniscus shows signs of extrusion prior to any loading which may alter biomechanical contact responses in both the medial and lateral compartments.

Flaws and cautions from the experimental data would highlight the reality that experimental testing is not always exact and repeatable. While the aim of this study was to compare directly to the values gathered from the patient specific cadaver tested, a certain level of human and test setup error must be taken into account to the measured data. The Tekscan instrumentation, while securely fastened during testing and a well-known and used piece of measuring equipment, has the potential to shift during testing. In addition to that, between each test scenario, the setup must be torn down in order to get adequate access to the surgical site to create each condition. This introduces a variable of sensor placement between each run as well. Even with covering the large majority of the tibial cartilage surface and using the same contact area for the computational contact area results, not all aspects of the contact during load could have been captured. The sensors are also known to not behave desirably on curved, surfaces which is the case for the tibial cartilage. All of these flaws of experimental testing is where having an FEA model can alleviate the pain points and produce straightforward, clear results for a problem at hand. However, validation to experimental data is an important and fundamental step to any good computational model.

Contact was modeled using the linear pressure-overclosure relationship. This proved to reach convergence while still yielding good results. While using exponential contact is more favorable for a higher accuracy solution, it could be said that for the 0° flexion model that exponential contact is not a necessity and potentially overkill. However, future models could utilize exponential contact modeling for best results.

With the creation of an FEA model, the effects of the presence of MFLs in the knee are now able to be seen at an extended level. It could be seen through the stress contours of Figure 44 for the pMFL in the results section that during the intact model – condition 1 – the pMFL is not highly stressed. However, during condition 2 where a LMPRA is present, the pMFL starts to see higher levels of stresses. This could be contributed to the pMFL now beginning to carry load while the root of the meniscus is detached. While still unknown in the literature and in practice what the true purpose of the MFLs are, this provides a convincing case to support the claim that the MFLs act as a secondary stabilizer for the lateral meniscus posterior root attachment, as stated by Geeslin et al [17].

CHAPTER 6 CONCLUSION

The purpose of this work was to validate a set of FEA models designed to predict the contact mechanics in primarily the lateral compartment of the knee for different loading conditions. Secondarily, contact mechanics were also observed in the medial compartment, which proved to uncover some potential flaws of the model. This work was compared against patient specific experimental data which showed agreeable results. The conditions studies looked at the contact area and peak pressure for intact, LMPRA, and LMPRA coupled with deficient MFLs. The computational model reported results of 446 mm^2 for contact area and 2.84 MPa for peak contact pressure at condition 1 – intact. These results were 14% less compared to those from the experimental study when comparing contact area and 22% less for peak contact pressure. Condition 2 – LMPRA – yielded contact area of 356 mm^2 and 2.89 MPa for peak contact pressure. Contact area came in 32% less than the experimental data and the peak contact pressure was reported at 12% less. Condition 3 – LMPRA with deficient MFLs – proved to have the most drastic differences in the experimental results, but less so in the computational results, compared to conditions 1 and 2. Contact area came in at 310 mm^2 and peak contact pressure was recorded at 2.98 MPa. These results were only 2% more than the experimental data for contact area but 35% less for the peak contact pressure. These results clearly show that the MFL has drastic stabilizing effects for the knee when a LMPRA is present. While surgical intervention is almost always still likely to occur when a LMPRA exists with the presence of MFLs, this work confirms that the MFLs will add a secondary stabilizer in the knee against injury.

Future work includes adding ACL tear, ACL reconstruction, and lateral meniscus posterior root repair conditions to the models developed. This would round out the work done by Geeslin et al, which this study is an extension of. Also, to continue the work done in the Geeslin study, each of these cases should be studied at varying flexion angles in addition to the 0° flexion angle this work was observed at. These would include 30°, 45°, 60°, and 90°. Additionally, models to study

the MFL in dynamic loading, rotational, and in shear will be able to still further explain the effects that the MFL has on the knee. Lastly, a study to observe the effects of the variability in MFL size and shape would be interesting in order to determine what genetic variables potentially have in the stability of the lateral meniscus posterior root.

BIBLIOGRAPHY

1. Bhatia S, LaPrade CM, Ellman MB, LaPrade RF. Meniscal Root Tears:Significance, Diagnosis, and Treatment. The American Journal of Sports Medicine 2014;**42**(12):3016-30 doi: 10.1177/0363546514524162[published Online First: Epub Date]|.
2. Miller MD, Wiesel SW. *Operative Techniques in Sports Medicine Surgery*: Wolters Kluwer Health, 2012.
3. Drake R, Vogl AW, Mitchell AWM. *Gray's Basic Anatomy E-Book*: Elsevier Health Sciences, 2016.
4. Total Meniscus Replacement Technology. (2015 SRN, 2017, from http://orthonika.com/total-meniscus-replacement/total-meniscus-replacement-technology.
5. Feucht MJ, Bigdon S, Bode G, et al. Associated tears of the lateral meniscus in anterior cruciate ligament injuries: risk factors for different tear patterns. Journal of Orthopaedic Surgery and Research 2015;**10**(1):34 doi: 10.1186/s13018-015-0184-x[published Online First: Epub Date]|.
6. De Smet AA, Blankenbaker DG, Kijowski R, Graf BK, Shinki K. MR Diagnosis of Posterior Root Tears of the Lateral Meniscus Using Arthroscopy as the Reference Standard. American Journal of Roentgenology 2009;**192**(2):480-86 doi: 10.2214/AJR.08.1300[published Online First: Epub Date]|.
7. Brody JM, Lin HM, Hulstyn MJ, Tung GA. Lateral Meniscus Root Tear and Meniscus Extrusion with Anterior Cruciate Ligament Tear. Radiology 2006;**239**(3):805-10 doi: 10.1148/radiol.2393050559[published Online First: Epub Date]|.
8. R L. Meniscal Root Tears. Secondary Meniscal Root Tears 2017.
9. Allaire R, Muriuki M, Gilbertson L, Harner CD. Biomechanical Consequences of a Tear of the Posterior Root of the Medial Meniscus: Similar to Total Meniscectomy. JBJS 2008;**90**(9):1922-31 doi: 10.2106/jbjs.g.00748[published Online First: Epub Date]|.
10. LaPrade CM, James EW, Cram TR, Feagin JA, Engebretsen L, LaPrade RF. Meniscal Root Tears:A Classification System Based on Tear Morphology. The American Journal of Sports Medicine 2015;**43**(2):363-69 doi: 10.1177/0363546514559684[published Online First: Epub Date]|.

11. Bonasia D.E. PP, D'Amello A., Cottino U., Rossi R. Meniscal root tear repair: why, when, and how? Orthopedic Reviews 2015;**7:5792**:34-39
12. Grood EMfAOS.
13. Moatshe G, Chahla, J., Slette, E., Engebretsen, L., & Laprade, R. F. . Posterior meniscal root injuries: A comprehensive review from anatomy to surgical treatment. Acta Orthopaedica 2016;**87**(5):452–58
14. LaPrade CM, Jansson KS, Dornan G, Smith SD, Wijdicks CA, LaPrade RF. Altered Tibiofemoral Contact Mechanics Due to Lateral Meniscus Posterior Horn Root Avulsions and Radial Tears Can Be Restored with in Situ Pull-Out Suture Repairs. JBJS 2014;**96**(6):471-79 doi: 10.2106/jbjs.l.01252[published Online First: Epub Date]|.
15. Amis AA, Gupte CM, Bull AMJ, Edwards A. Anatomy of the posterior cruciate ligament and the meniscofemoral ligaments. Knee Surgery, Sports Traumatology, Arthroscopy 2006;**14**(3):257-63 doi: 10.1007/s00167-005-0686-x[published Online First: Epub Date]|.
16. Microfracture surgery. (2017 SIW, The Free Encyclopedia. Retrieved 19:52, November 5, 2017, from https://en.wikipedia.org/w/index.php?title=Microfracture_surgery&oldid=802535486.
17. Geeslin AG CD, Turnbull TL, Dornan GJ, Fuso FA, LaPrade RF. Influence of lateral meniscal posterior root avulsions and the meniscofemoral ligaments on tibiofemoral contact mechanics. Knee Surg Sports Traumatol Arthrosc 2015 doi: 10.1007/s00167-015-3742-1[published Online First: Epub Date]|.
18. Bintoudi A, Natsis K, Tsitouridis I. Anterior and Posterior Meniscofemoral Ligaments: MRI Evaluation. Anatomy Research International 2012;**2012**:5 doi: 10.1155/2012/839724[published Online First: Epub Date]|.
19. Gupte CM, Smith A, McDermott ID, Bull AMJ, Thomas RD, Amis AA. Meniscofemoral ligaments revisited. ANATOMICAL STUDY, AGE CORRELATION AND CLINICAL IMPLICATIONS 2002;**84-B**(6):846-51 doi: 10.1302/0301-620x.84b6.13110[published Online First: Epub Date]|.
20. Forkel P, Herbort M, Sprenker F, Metzlaff S, Raschke M, Petersen W. The Biomechanical Effect of a Lateral Meniscus Posterior Root Tear With and Without Damage to the Meniscofemoral Ligament: Efficacy of Different Repair Techniques. Arthroscopy

2014;**30**(7):833-40 doi: 10.1016/j.arthro.2014.02.040[published Online First: Epub Date]|.

21. Zielinska B, Haut Donahue TL. 3D Finite Element Model of Meniscectomy: Changes in Joint Contact Behavior. Journal of Biomechanical Engineering 2005;**128**(1):115-23 doi: 10.1115/1.2132370[published Online First: Epub Date]|.
22. Bao HRC ZD, Gong H, Gu GS. The effect of complete radial lateral meniscus posterior root tear on the knee contact mechanics: a finite element analysis J Orthop Sci 2013;**18**:256-63
23. Mootanah R, Imhauser CW, Reisse F, et al. Development and validation of a computational model of the knee joint for the evaluation of surgical treatments for osteoarthritis. Computer Methods in Biomechanics and Biomedical Engineering 2014;**17**(13):1502-17 doi: 10.1080/10255842.2014.899588[published Online First: Epub Date]|.
24. Kiapour A, Kiapour AM, Kaul V, et al. Finite Element Model of the Knee for Investigation of Injury Mechanisms: Development and Validation. Journal of Biomechanical Engineering 2013;**136**(1):011002-02-14 doi: 10.1115/1.4025692[published Online First: Epub Date]|.
25. Peña E, Calvo B, Martínez MA, Doblaré M. A three-dimensional finite element analysis of the combined behavior of ligaments and menisci in the healthy human knee joint. Journal of Biomechanics 2005;**39**(9):1686-701 doi: 10.1016/j.jbiomech.2005.04.030[published Online First: Epub Date]|.
26. Weiss JA, Maker BN, Govindjee S. Finite element implementation of incompressible, transversely isotropic hyperelasticity. Computer Methods in Applied Mechanics and Engineering 1996;**135**(1):107-28 doi: https://doi.org/10.1016/0045-7825(96)01035-3[published Online First: Epub Date]|.
27. Weiss JA, Gardiner JC, Ellis BJ, Lujan TJ, Phatak NS. Three-dimensional finite element modeling of ligaments: Technical aspects. Medical Engineering and Physics 2005;**27**(10):845-61 doi: 10.1016/j.medengphy.2005.05.006[published Online First: Epub Date]|.
28. Fox AJS, Wanivenhaus F, Burge AJ, Warren RF, Rodeo SA. The human meniscus: A review of anatomy, function, injury, and advances in treatment. Clinical Anatomy 2015;**28**(2):269-87 doi: 10.1002/ca.22456[published Online First: Epub Date]|.

29. Blankevoort L, Kuiper JH, Huiskes R, Grootenboer HJ. Articular contact in a three-dimensional model of the knee. Journal of Biomechanics 1991;**24**(11):1019-31 doi: https://doi.org/10.1016/0021-9290(91)90019-J[published Online First: Epub Date]|.
30. Leyland T. Biomechanics of Joints, Ligaments and Tendons. Secondary Biomechanics of Joints, Ligaments and Tendons 2009. http://www.sfu.ca/~leyland/Kin201 Files/Connective.pdf.
31. Kim N-H. Chapter 3: Finite element analysis for nonlinear elastic problems. Secondary Chapter 3: Finite element analysis for nonlinear elastic problems 2017. http://www2.mae.ufl.edu/nkim/egm6352/Chap3.pdf.
32. Abaqus Analysis User's Guide (6.14). N.p. ndWJ.
33. dhondt g. Node-to-Face Penalty Contact. Secondary Node-to-Face Penalty Contact 2014. http://web.mit.edu/calculix_v2.7/CalculiX/ccx_2.7/doc/ccx/node111.html.
34. dhondt g. Face-to-Face Penalty Contact. Secondary Face-to-Face Penalty Contact 2014. http://web.mit.edu/calculix_v2.7/CalculiX/ccx_2.7/doc/ccx/node112.html.
35. Pressure Mapping Sensor 4000. Secondary Pressure Mapping Sensor 4000. https://www.tekscan.com/products-solutions/pressure-mapping-sensors/4000?tab=specifications.
36. Tekscan. Comparison of Interface Pressure Measurement Options: Review of Load Cells, Pressure Indicating Film, and Tactile Pressure Sensors for Improvement of Research and Quality Control, 2008.
37. Fedorov A. BR, Kalpathy-Cramer J., Finet J., Fillion-Robin J-C., Pujol S., Bauer C., Jennings D., Fennessy F., Sonka M., Buatti J., Aylward S.R., Miller J.V., Pieper S., Kikinis R. 3D Slicer as an Image Computing Platform for the Quantitative Imaging Network. Magnetic Resonance Imaging. 2012 Nov;30(9):1323-41. PMID: 22770690. Secondary.
38. P. Cignoni MC, M. Corsini, M. Dellepiane, F. Ganovelli, G. Ranzuglia , Tool MaO-SMP, Sixth Eurographics Italian Chapter Conference p-, 2008.
39. How Does Altair Make a Difference? (n.d.). Retrieved November 13, from http://www.altair.com/. Secondary.

APPENDICES

Appendix A Input File – Condition 1 (Intact)

```
**Abaqus Input file
**Erika Fojtik
*HEADING
CONDITION 1, 0DEG FLEXION, HYPERELASTIC LIGAMENTS
**
**RIGID BODYs
**NODES AND ELEMENTS DEFINED*****************************************
*INCLUDE, INPUT = c1v1.txt
**
**MATERIALS DEFINED***************************************************
**
*MATERIAL, NAME = BONE
*ELASTIC, TYPE = ISOTROPIC
20e3, .3, 0
*SOLID SECTION, ELSET=TIBIA, MATERIAL=BONE
*SOLID SECTION, ELSET=FEMUR, MATERIAL=BONE
**
*RIGID BODY, ELSET = TIBIA, REF NODE = 1, ROT NODE = 2
*RIGID BODY, ELSET = FEMUR, REF NODE = 3, ROT NODE = 4
**
*MATERIAL, NAME = ACL
*HYPERELASTIC, NEO HOOKE
1.95,.017
*SOLID SECTION, ELSET=ACL, MATERIAL=ACL
*MATERIAL, NAME = PCL
**
*HYPERELASTIC, NEO HOOKE
3.25,.010
*SOLID SECTION, ELSET=PCL, MATERIAL=PCL
*SOLID SECTION, ELSET=pMFL, MATERIAL=PCL
**
*MATERIAL, NAME = CARTILAGE
*ELASTIC, TYPE = ISOTROPIC
        15.0, .475
*SOLID SECTION, ELSET=FEM_CART, MATERIAL=CARTILAGE
*SOLID SECTION, ELSET=TIB_CART, MATERIAL=CARTILAGE
**
*MATERIAL, NAME = MENISCUS
*ELASTIC, TYPE = ENGINEERING CONSTANTS
20,120,20,.3,.2,.3,57.7,57.7
8.33,
*ORIENTATION, NAME=LMO, SYSTEM= CYLINDRICAL
-20.981,7.094,-4.649,-20.981,7.094, -3
*SOLID SECTION, ELSET=LM, MATERIAL=MENISCUS, ORIENTATION=LMO
```

```
*ORIENTATION, NAME=MMO, SYSTEM= CYLINDRICAL
22.125, 7.224,-4.840, 22.125, 7.224, -3
*SOLID SECTION, ELSET=MM, MATERIAL=MENISCUS, ORIENTATION=MMO
**
**CONTACTS AND SURFACES DEFINED**************************************
**
**
*TIE, NAME=FEM CART TO FEMUR, POSITION TOLERANCE = .3
FEM_CART, FEMUR
*TIE, NAME=TIB CART TO TIBIA, POSITION TOLERANCE = .27
TIB_CART, TIBIA
**
**Swap dep <-> ind for tib_cart <-> fem_cart
*CONTACT PAIR, INTERACTION=CART, TYPE=SURFACE TO SURFACE, ADJUST=.01
TIB_CART, FEM_CART
*SURFACE INTERACTION, NAME=CART
*SURFACE BEHAVIOR, PRESSURE-OVERCLOSURE = LINEAR
75
**
*TIE, NAME=ACL TO TIB, POSITION TOLERANCE = .2
ACL_TIB, TIB_ACL
*TIE, NAME = PCL TO TIB, POSITION TOLERANCE = .2
PCL_TIB, TIB_PCL
*TIE, NAME = ACL TO FEM, POSITION TOLERANCE = .3
ACL_FEM, FEM_ACL
*TIE, NAME = PCL TO FEM, POSITION TOLERANCE = .25
PCL_FEM, FEM_PCL
**
*TIE, NAME=LMPR, POSITION TOLERANCE = .2
LMPR, TIBIA
*TIE, NAME=LMAR, POSITION TOLERANCE = .25
LMAR, TIBIA
*TIE, NAME=MMPR, POSITION TOLERANCE = .15
MMPR, TIBIA
*TIE, NAME=MMAR, POSITION TOLERANCE = .15
MMAR, TIBIA
**
*CONTACT PAIR, INTERACTION=MMENISCUS_TIB, TYPE=SURFACE TO SURFACE, ADJUST=.01
TIB_CART, MM
*SURFACE INTERACTION, NAME=MMENISCUS_TIB
*SURFACE BEHAVIOR, PRESSURE-OVERCLOSURE = LINEAR
75
*CONTACT PAIR, INTERACTION=MMENISCUS_FEM, TYPE=SURFACE TO SURFACE, ADJUST=.01
FEM_CART, MM
*SURFACE INTERACTION, NAME=MMENISCUS_FEM
*SURFACE BEHAVIOR, PRESSURE-OVERCLOSURE = LINEAR
75
```

```
*CONTACT PAIR, INTERACTION=LMENISCUS_TIB, TYPE=SURFACE TO SURFACE, ADJUST=.01
TIB_CART, LM
*SURFACE INTERACTION, NAME=LMENISCUS_TIB
*SURFACE BEHAVIOR, PRESSURE-OVERCLOSURE = LINEAR
75
*CONTACT PAIR, INTERACTION=LMENISCUS_FEM, TYPE=SURFACE TO SURFACE, ADJUST=.01
FEM_CART, LM
*SURFACE INTERACTION, NAME=LMENISCUS_FEM
*SURFACE BEHAVIOR, PRESSURE-OVERCLOSURE = LINEAR
75
**
*TIE, NAME=pMFL TO LM, POSITION TOLERANCE = .25
pMFL_LM, LM_pMFL
*TIE, NAME=pMFL TO FEM, POSITION TOLERANCE = .2
pMFL_FEM, FEM_pMFL
**
**BOUNDARY CONDITIONS AND LOADS**************************************
*BOUNDARY
1,1,3,0
2,1,1,0
2,3,3,0
*BOUNDARY
3,1,2,0
4,1,3,0
**
**HISTORY FILES*****************************************************
*STEP,NLGEOM
*STATIC
        .1,1
*CLOAD
3,3,-1000
****
*NODE FILE
 U, RF
*EL FILE
 S, E
*CONTACT FILE
CAREA, CSTR
**
*END STEP
*****
```

Appendix B Input File – Condition 2 (LMPRA)

```
**Abaqus Input file
**Erika Fojtik
*HEADING
CONDITION 2, 0DEG FLEXION, HYPERELASTIC LIGAMENTS
**
**RIGID BODYs
**NODES AND ELEMENTS DEFINED*****************************************
*INCLUDE, INPUT = c2v1.txt
**
**MATERIALS DEFINED***************************************************
**
*MATERIAL, NAME = BONE
*ELASTIC, TYPE = ISOTROPIC
20e3, .3, 0
*SOLID SECTION, ELSET=TIBIA, MATERIAL=BONE
*SOLID SECTION, ELSET=FEMUR, MATERIAL=BONE
**
*RIGID BODY, ELSET = TIBIA, REF NODE = 1, ROT NODE = 2
*RIGID BODY, ELSET = FEMUR, REF NODE = 3, ROT NODE = 4
**
*MATERIAL, NAME = ACL
*HYPERELASTIC, NEO HOOKE
1.95,.017
*SOLID SECTION, ELSET=ACL, MATERIAL=ACL
*MATERIAL, NAME = PCL
**
*HYPERELASTIC, NEO HOOKE
3.25,.010
*SOLID SECTION, ELSET=PCL, MATERIAL=PCL
*SOLID SECTION, ELSET=pMFL, MATERIAL=PCL
**
*MATERIAL, NAME = CARTILAGE
*ELASTIC, TYPE = ISOTROPIC
        15.0, .475
*SOLID SECTION, ELSET=FEM_CART, MATERIAL=CARTILAGE
*SOLID SECTION, ELSET=TIB_CART, MATERIAL=CARTILAGE
**
*MATERIAL, NAME = MENISCUS
*ELASTIC, TYPE = ENGINEERING CONSTANTS
20,120,20,.3,.2,.3,57.7,57.7
8.33,
*ORIENTATION, NAME=LMO, SYSTEM= CYLINDRICAL
-20.981,7.094,-4.649,-20.981,7.094, -3
*SOLID SECTION, ELSET=LM, MATERIAL=MENISCUS, ORIENTATION=LMO
```

```
*ORIENTATION, NAME=MMO, SYSTEM= CYLINDRICAL
22.125, 7.224,-4.840, 22.125, 7.224, -3
*SOLID SECTION, ELSET=MM, MATERIAL=MENISCUS, ORIENTATION=MMO
**
**CONTACTS AND SURFACES DEFINED**************************************
**
**
*TIE, NAME=FEM CART TO FEMUR, POSITION TOLERANCE = .3
FEM_CART, FEMUR
*TIE, NAME=TIB CART TO TIBIA, POSITION TOLERANCE = .27
TIB_CART, TIBIA
**
**Swap dep <-> ind for tib_cart <-> fem_cart
*CONTACT PAIR, INTERACTION=CART, TYPE=SURFACE TO SURFACE, ADJUST=.01
TIB_CART, FEM_CART
*SURFACE INTERACTION, NAME=CART
*SURFACE BEHAVIOR, PRESSURE-OVERCLOSURE = LINEAR
75
**
*TIE, NAME=ACL TO TIB, POSITION TOLERANCE = .2
ACL_TIB, TIB_ACL
*TIE, NAME = PCL TO TIB, POSITION TOLERANCE = .2
PCL_TIB, TIB_PCL
*TIE, NAME = ACL TO FEM, POSITION TOLERANCE = .3
ACL_FEM, FEM_ACL
*TIE, NAME = PCL TO FEM, POSITION TOLERANCE = .25
PCL_FEM, FEM_PCL
**
**************************
**Condition 2 - LMPRA
**TIE, NAME=LMPR, POSITION TOLERANCE = .2
**LMPR, TIBIA
**************************
*TIE, NAME=LMAR, POSITION TOLERANCE = .25
LMAR, TIBIA
*TIE, NAME=MMPR, POSITION TOLERANCE = .15
MMPR, TIBIA
*TIE, NAME=MMAR, POSITION TOLERANCE = .15
MMAR, TIBIA
**
*CONTACT PAIR, INTERACTION=MMENISCUS_TIB, TYPE=SURFACE TO SURFACE, ADJUST=.01
TIB_CART, MM
*SURFACE INTERACTION, NAME=MMENISCUS_TIB
*SURFACE BEHAVIOR, PRESSURE-OVERCLOSURE = LINEAR
75
*CONTACT PAIR, INTERACTION=MMENISCUS_FEM, TYPE=SURFACE TO SURFACE, ADJUST=.01
FEM_CART, MM
```

```
*SURFACE INTERACTION, NAME=MMENISCUS_FEM
*SURFACE BEHAVIOR, PRESSURE-OVERCLOSURE = LINEAR
75
*CONTACT PAIR, INTERACTION=LMENISCUS_TIB, TYPE=SURFACE TO SURFACE, ADJUST=.01
TIB_CART, LM
*SURFACE INTERACTION, NAME=LMENISCUS_TIB
*SURFACE BEHAVIOR, PRESSURE-OVERCLOSURE = LINEAR
75
*CONTACT PAIR, INTERACTION=LMENISCUS_FEM, TYPE=SURFACE TO SURFACE, ADJUST=.01
FEM_CART, LM
*SURFACE INTERACTION, NAME=LMENISCUS_FEM
*SURFACE BEHAVIOR, PRESSURE-OVERCLOSURE = LINEAR
75
**
*TIE, NAME=pMFL TO LM, POSITION TOLERANCE = .25
pMFL_LM, LM_pMFL
*TIE, NAME=pMFL TO FEM, POSITION TOLERANCE = .2
pMFL_FEM, FEM_pMFL
**
**BOUNDARY CONDITIONS AND LOADS**************************************
*BOUNDARY
1,1,3,0
2,1,1,0
2,3,3,0
*BOUNDARY
3,1,2,0
4,1,3,0
**
**HISTORY FILES*************************************************
*STEP,NLGEOM
*STATIC
        .1,1
*CLOAD
3,3,-1000
****
*NODE FILE
 U, RF
*EL FILE
 S, E
*CONTACT FILE
CAREA, CSTR
**
*END STEP
*****
```

Appendix C Input File – Condition 3 (LMPRA + Deficient MFL)

```
**Abaqus Input file
**Erika Fojtik
*HEADING
CONDITION 3, 0DEG FLEXION, HYPERELASTIC LIGAMENTS
**
**RIGID BODYs
**NODES AND ELEMENTS DEFINED*****************************************
*INCLUDE, INPUT = C3V3.txt
**
**MATERIALS DEFINED**************************************************
**
*MATERIAL, NAME = BONE
*ELASTIC, TYPE = ISOTROPIC
20e3, .3, 0
*SOLID SECTION, ELSET=TIBIA, MATERIAL=BONE
*SOLID SECTION, ELSET=FEMUR, MATERIAL=BONE
**
*RIGID BODY, ELSET = TIBIA, REF NODE = 1, ROT NODE = 2
*RIGID BODY, ELSET = FEMUR, REF NODE = 3, ROT NODE = 4
**
*MATERIAL, NAME = ACL
*HYPERELASTIC, NEO HOOKE
1.95,.017
*SOLID SECTION, ELSET=ACL, MATERIAL=ACL
*MATERIAL, NAME = PCL
*HYPERELASTIC, NEO HOOKE
3.25,.010
*SOLID SECTION, ELSET=PCL, MATERIAL=PCL
**SOLID SECTION, ELSET=pMFL, MATERIAL=PCL
**
*MATERIAL, NAME = CARTILAGE
*ELASTIC, TYPE = ISOTROPIC
        15.0, .475
*SOLID SECTION, ELSET=FEM_CART, MATERIAL=CARTILAGE
*SOLID SECTION, ELSET=TIB_CART, MATERIAL=CARTILAGE
**
*MATERIAL, NAME = MENISCUS
*ELASTIC, TYPE = ENGINEERING CONSTANTS
20,120,20,.3,.2,.3,57.7,57.7
8.33,
*ORIENTATION, NAME=LMO, SYSTEM= CYLINDRICAL
-20.981,7.094,-4.649,-20.981,7.094, -3
*SOLID SECTION, ELSET=LM, MATERIAL=MENISCUS, ORIENTATION=LMO
*ORIENTATION, NAME=MMO, SYSTEM= CYLINDRICAL
```

```
22.125, 7.224,-4.840, 22.125, 7.224, -3
*SOLID SECTION, ELSET=MM, MATERIAL=MENISCUS, ORIENTATION=MMO
**
**CONTACTS AND SURFACES DEFINED**************************************
**
**
*TIE, NAME=FEM CART TO FEMUR, POSITION TOLERANCE = .3
FEM_CART, FEMUR
*TIE, NAME=TIB CART TO TIBIA, POSITION TOLERANCE = .27
TIB_CART, TIBIA
**
**Swap dep <-> ind for tib_cart <-> fem_cart
*CONTACT PAIR, INTERACTION=CART, TYPE=SURFACE TO SURFACE, ADJUST=.01
TIB_CART, FEM_CART
*SURFACE INTERACTION, NAME=CART
*SURFACE BEHAVIOR, PRESSURE-OVERCLOSURE = LINEAR
75
**
*TIE, NAME=ACL TO TIB, POSITION TOLERANCE = .2
ACL_TIB, TIB_ACL
*TIE, NAME = PCL TO TIB, POSITION TOLERANCE = .2
PCL_TIB, TIB_PCL
*TIE, NAME = ACL TO FEM, POSITION TOLERANCE = .3
ACL_FEM, FEM_ACL
*TIE, NAME = PCL TO FEM, POSITION TOLERANCE = .25
PCL_FEM, FEM_PCL
**
**TIE, NAME=LMPR, POSITION TOLERANCE = .2
**LMPR, TIBIA
*TIE, NAME=LMAR, POSITION TOLERANCE = .25
LMAR, TIBIA
*TIE, NAME=MMPR, POSITION TOLERANCE = .15
MMPR, TIBIA
*TIE, NAME=MMAR, POSITION TOLERANCE = .15
MMAR, TIBIA
**
*CONTACT PAIR, INTERACTION=MMENISCUS_TIB, TYPE=SURFACE TO SURFACE, ADJUST=.01
TIB_CART, MM
*SURFACE INTERACTION, NAME=MMENISCUS_TIB
*SURFACE BEHAVIOR, PRESSURE-OVERCLOSURE = LINEAR
75
*CONTACT PAIR, INTERACTION=MMENISCUS_FEM, TYPE=SURFACE TO SURFACE, ADJUST=.01
FEM_CART, MM
*SURFACE INTERACTION, NAME=MMENISCUS_FEM
*SURFACE BEHAVIOR, PRESSURE-OVERCLOSURE = LINEAR
75
*CONTACT PAIR, INTERACTION=LMENISCUS_TIB, TYPE=SURFACE TO SURFACE, ADJUST=.01
```

```
TIB_CART, LM
*SURFACE INTERACTION, NAME=LMENISCUS_TIB
*SURFACE BEHAVIOR, PRESSURE-OVERCLOSURE = LINEAR
75
*CONTACT PAIR, INTERACTION=LMENISCUS_FEM, TYPE=SURFACE TO SURFACE, ADJUST=.01
FEM_CART, LM
*SURFACE INTERACTION, NAME=LMENISCUS_FEM
*SURFACE BEHAVIOR, PRESSURE-OVERCLOSURE = LINEAR
75
**
**TIE, NAME=pMFL TO LM, POSITION TOLERANCE = .25
**pMFL_LM, LM_pMFL
**TIE, NAME=pMFL TO FEM, POSITION TOLERANCE = .2
**pMFL_FEM, FEM_pMFL
**
**BOUNDARY CONDITIONS AND LOADS**************************************
*BOUNDARY
1,1,3,0
2,1,1,0
2,3,3,0
*BOUNDARY
3,1,2,0
4,1,3,0
**
**HISTORY FILES************************************************************
*STEP,NLGEOM
*STATIC
                .1,1
*CLOAD
3,3,-1000
****
*NODE FILE
 U, RF
*EL FILE
 S, E
*CONTACT FILE
CAREA, CSTR
**
*END STEP
*****
```

Appendix D Additional Results Images

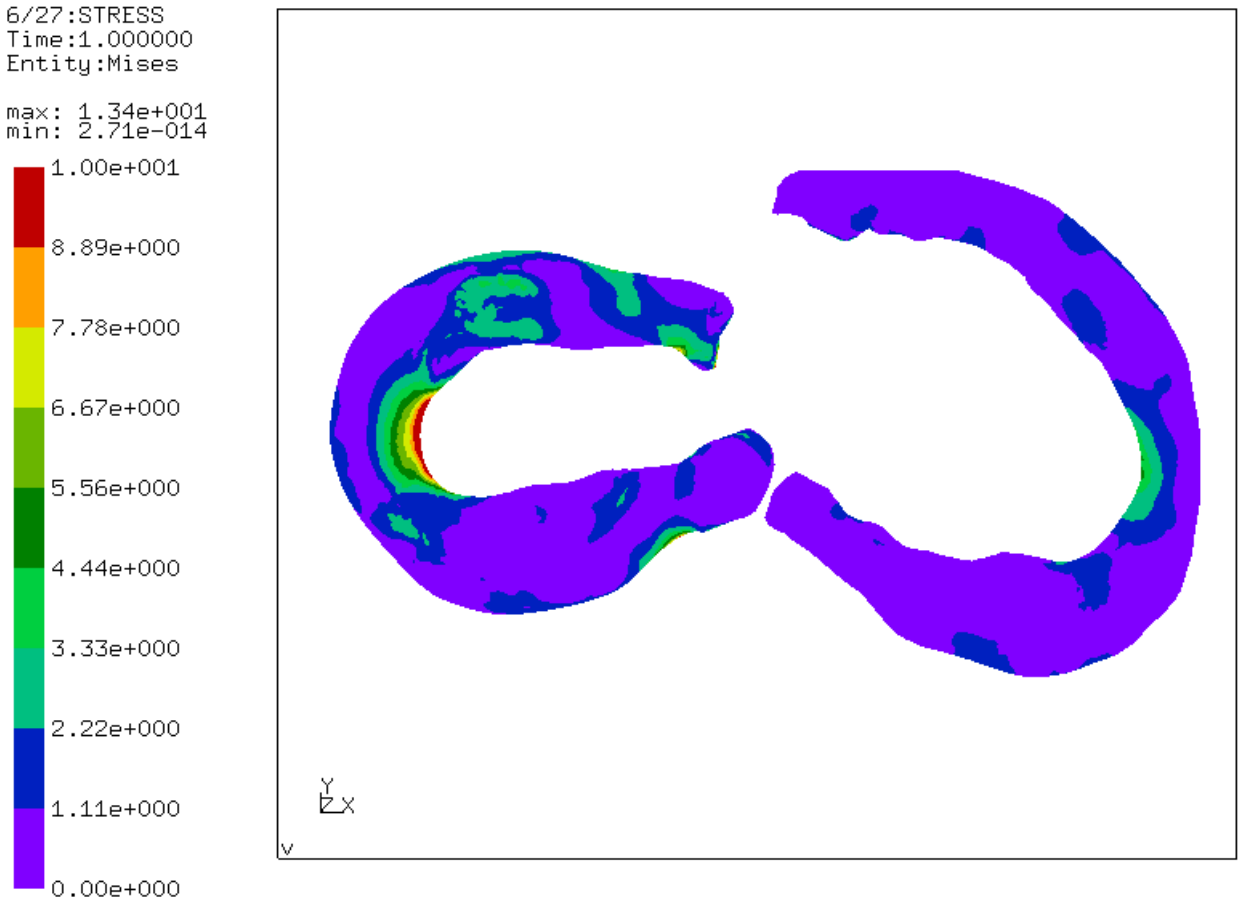

Figure 47: Stress distribution (Von Mises) of the lateral (left) and medial (right) menisci for Condition 1 - Intact.

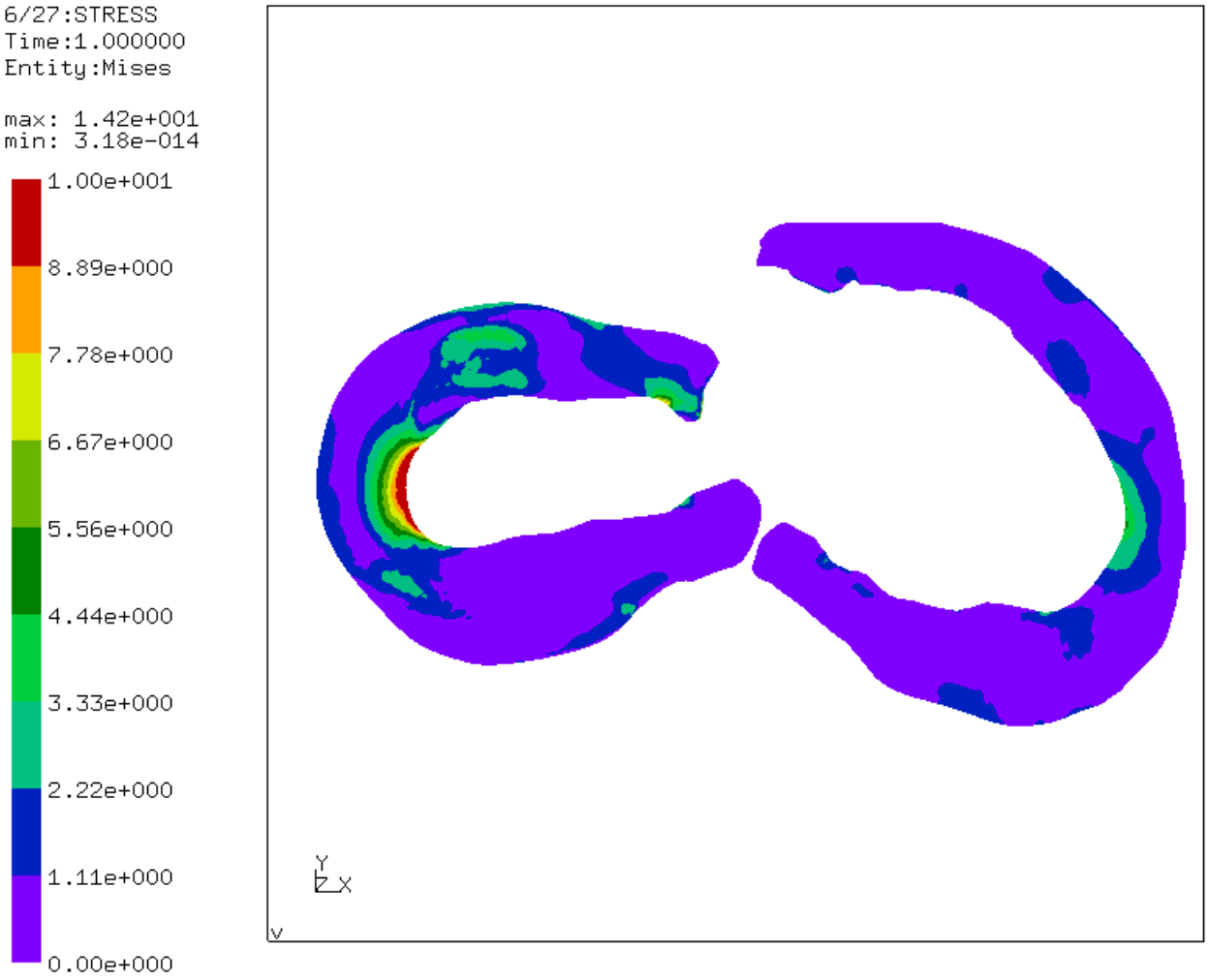

Figure 48: Stress distribution (Von Mises) of the lateral (left) and medial (right) menisci for Condition 2 - LMPRA.

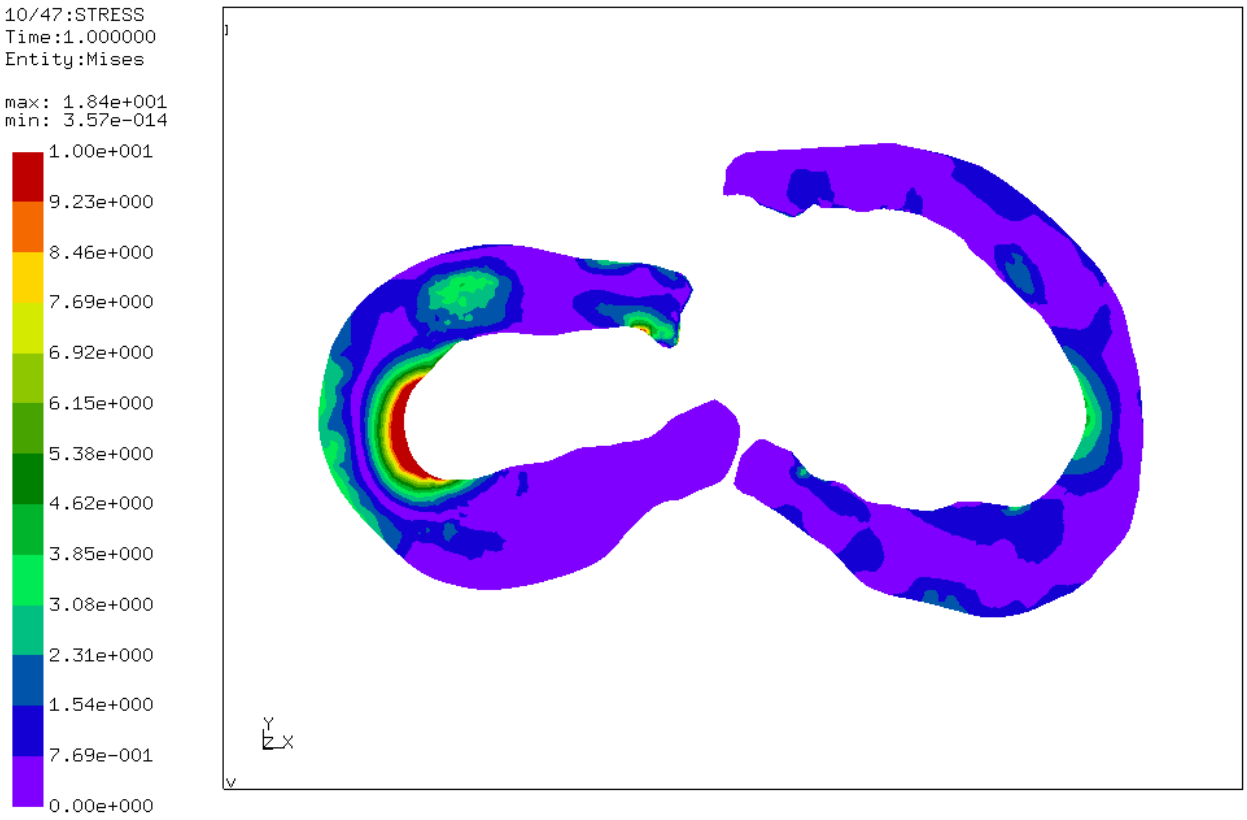

Figure 49: Stress distribution (Von Mises) of the lateral (left) and medial (right) menisci for Condition 3 - LMPRA and deficient MFL.